Modeling the Dust Properties of z ~ 6 Quasars with ART2—All-Wavelength Radiative Transfer with Adaptive Refinement Tree

The Astrophysical Journal, 678:41–63, 2008 May 1

MODELING THE DUST PROPERTIES OF $z \sim 6$ QUASARS WITH ART^2—ALL-WAVELENGTH RADIATIVE TRANSFER WITH ADAPTIVE REFINEMENT TREE

Yuexing Li,[1] Philip F. Hopkins,[1] Lars Hernquist,[1] Douglas P. Finkbeiner,[1] Thomas J. Cox,[1]
Volker Springel,[2] Linhua Jiang,[3] Xiaohui Fan,[3] and Naoki Yoshida[4]
Received 2007 June 27; accepted 2007 December 20

ABSTRACT

The detection of large quantities of dust in $z \sim 6$ quasars by infrared and radio surveys presents puzzles for the formation and evolution of dust in these early systems. Previously, Li et al. showed that luminous quasars at $z \gtrsim 6$ can form through hierarchical mergers of gas-rich galaxies, and that these systems are expected to evolve from starburst through quasar phases. Here, we calculate the dust properties of simulated quasars and their progenitors using a three-dimensional Monte Carlo radiative transfer code, ART^2 (All-wavelength Radiative Transfer with Adaptive Refinement Tree). ART^2 incorporates a radiative equilibrium algorithm which treats dust emission self-consistently, an adaptive grid method which can efficiently cover a large dynamic range in both spatial and density scales, a multiphase model of the interstellar medium which accounts for the observed scaling relations of molecular clouds, and a supernova-origin model for dust which can explain the existence of dust in cosmologically young objects. By applying ART^2 to the hydrodynamic simulations of Li et al., we reproduce the observed spectral energy distribution (SED) and inferred dust properties of SDSS J1148+5251, the most distant Sloan quasar. We find that the dust and infrared emission are closely associated with the formation and evolution of the quasar host. The system evolves from a cold to a warm ultraluminous infrared galaxy (ULIRG) owing to heating and feedback from stars and the active galactic nucleus (AGN). Furthermore, the AGN activity has significant implications for the interpretation of observation of the hosts. Our results suggest that vigorous star formation in merging progenitors is necessary to reproduce the observed dust properties of $z \sim 6$ quasars, supporting a merger-driven origin for luminous quasars at high redshifts and the starburst-to-quasar evolutionary hypothesis.

Subject headings: galaxies: formation — galaxies: evolution — galaxies: high-redshift — galaxies: starburst — infrared: galaxies — radiative transfer — dust, extinction — ISM: individual (SDSS J1148+5251)

1. INTRODUCTION

High-redshift quasars are important for understanding the formation and evolution of galaxies and supermassive black holes (SMBHs) in the early universe. In the past few years, nearly two dozen luminous quasars have been discovered by the Sloan Digital Sky Survey (SDSS; York et al. 2000) and the Canada-France High-z Quasar Survey (CFHQS; Willott et al. 2007) at $z \sim 6$, corresponding to a time when the universe was less than a billion years old (Fan et al. 2003, 2004, 2006a, 2006b). As summarized by Fan (2006), these quasars are rare ($\sim 10^{-9}$ Mpc^{-3} comoving); believed to be powered by SMBHs with masses $\sim 10^9\ M_\odot$ (e.g., Willott et al. 2003; Barth et al. 2003); reside near the end of the epoch of reionization, as indicated by Gunn-Peterson absorption troughs (Gunn & Peterson 1965) in their spectra; and have similar spectral energy distributions (SEDs) and comparable metallicity to lower redshift counterparts (e.g., Elvis et al. 1994; Glikman et al. 2006; Richards et al. 2006; Hopkins et al. 2007d), implying the early presence of "mature" quasars and the formation of their hosts in rapid starbursts at even higher redshifts ($z \gtrsim 10$).

Follow-up, multiwavelength observations have been carried out for these $z \sim 6$ quasars, from X-ray (e.g., Brandt et al. 2002; Strateva et al. 2005; Vignali et al. 2005; Steffen et al. 2006; Shemmer et al. 2005, 2006), to optical /infrared (e.g., Barth et al. 2003; Pentericci et al. 2003; Freudling et al. 2003; White et al. 2005; Willott et al. 2005; Hines et al. 2006), and radio wavelengths (e.g., Carilli et al. 2001, 2004; Bertoldi et al. 2003b; Walter et al. 2003; Wang et al. 2007). A noteworthy result of these studies is their detection of dust in these high-redshift objects. In particular, deep infrared and radio surveys (e.g., Robson et al. 2004; Bertoldi et al. 2003a; Carilli et al. 2004; Charmandaris et al. 2004; Beelen et al. 2006; Hines et al. 2006) have revealed a large amount of cold dust in SDSS J1148+5251 (hereafter J1148+5251), the most distant Sloan quasar detected at redshift $z = 6.42$ (Fan et al. 2003). The dust mass is estimated to be $\sim(1\text{–}7) \times 10^8\ M_\odot$. The detection of dust is also reported in the first four CFHQS quasars at $z > 6$, including the new record holder CFHQS J2329−0301 at $z = 6.43$ (Willott et al. 2007). Maiolino et al. (2004) argue, from the observed dust extinction curve of SDSS J1048+4637 at $z = 6.2$, that the dust in these high-z systems may be produced by supernovae.

Jiang et al. (2006) have performed a comprehensive study of 13 $z \sim 6$ quasars by combining new *Spitzer* observations with existing multiband data. It appears that nearly all 13 of these quasars exhibit prominent infrared bumps around both $\lambda \sim 3$ and $\lambda \sim 50$ μm. In a dusty galaxy, most of the radiation from newly formed stars or an active galactic nucleus (AGN) is absorbed by dust and reemitted at infrared wavelengths. The SEDs of star-forming galaxies typically peak at 50–80 μm (rest frame) and can be approximated by a modified blackbody spectrum with dust temperatures below 100 K (e.g., Dunne & Eales 2001), while in quasars, some dust can be heated directly by the AGN to temperatures up to 1200 K (e.g., Glikman et al. 2006) and dominate

[1] Harvard-Smithsonian Center for Astrophysics, Harvard University, 60 Garden Street, Cambridge, MA 02138.
[2] Max-Planck-Institute for Astrophysics, Karl-Schwarzschild-Strasse 1, 85740 Garching, Germany.
[3] Department of Astronomy, University of Arizona, 933 North Cherry Avenue, Tucson, AZ 85721.
[4] Nagoya University, Department of Physics, Nagoya, Aichi 464-8602, Japan.

the near- to mid-IR emission. Therefore, the observations by Jiang et al. (2006) indicate the presence of large amounts of both hot and cold dust in these high-z systems.

However, the nature of the dust, and its formation and evolution in the context of the quasar host, are unclear. For example, the dust distribution is unknown. It has been suggested that the hot dust lies in the central regions and is heated by an AGN to produce near-IR (NIR) emission (Rieke & Lebofsky 1981; Polletta et al. 2000; Haas et al. 2003), while the warm and cold dust can extend to a few kiloparsecs and dominate at mid-IR (MIR) and far-IR (FIR) wavelengths (Polletta et al. 2000; Nenkova et al. 2002; Siebenmorgen et al. 2005). However, the relative importance of heating by stars and AGN activity is uncertain. This is essential to an accurate determination of the star formation rate (SFR), but cannot be inferred simply from observed SEDs. Currently, the most common method used to derive a star formation rate is to assume that most of the FIR luminosity comes from young stars. However, if the FIR luminosity is mainly contributed by an AGN, then the SFR would be substantially reduced. Finally, it is not known how the SED and dust content of a quasar and its host evolve with time.

In order to address these questions, we must combine a model for the formation of a quasar with radiative transfer calculations that treat dust emission self-consistently, to follow the physical properties, environment, and evolution of quasar hosts and their dust content.

Earlier (Li et al. 2007), we developed a quasar formation model which self-consistently accounts for black hole growth, star formation, quasar activity, and host spheroid formation in the context of hierarchical structure formation. We employed a set of multiscale simulations that included large-scale cosmological simulations and galaxy mergers on galactic scales, together with a self-regulated model for black hole growth, to produce a luminous quasar at $z \sim 6.5$, which has a black hole mass ($\sim 2 \times 10^9\ M_\odot$) and a number of properties similar to J1148+5251 (Fan et al. 2003). In our scenario, luminous, high-redshift quasars form in massive halos that originate from rare density peaks in the standard ΛCDM cosmology, and they grow through hierarchical mergers of gas-rich galaxies. Gravitational torques excited in these mergers trigger large inflows of gas and produce strong shocks that result in intense starbursts (Hernquist 1989; Barnes & Hernquist 1991, 1992, 1996; Hernquist & Mihos 1995; Mihos & Hernquist 1996) and fuel rapid black hole accretion (Di Matteo et al. 2005; Springel et al. 2005a). Moreover, feedback from the accreting black hole disperses the obscuring material, briefly yielding an optically visible quasar (Hopkins et al. 2005a, 2005b, 2005c, 2006), and regulating the $M_{\rm BH}$-σ correlation between the SMBHs and host galaxies (Di Matteo et al. 2005; Robertson et al. 2006). In this picture, quasars are, therefore, descendents of starburst galaxies (Sanders et al. 1988; Norman & Scoville 1988; Scoville 2003).

To make detailed contact with observations of $z \sim 6$ quasars, it is necessary to theoretically predict the SEDs of these systems and how they evolve with time. Solving radiation transport in dusty, starbursting quasars is, however, difficult owing to the nonlocality of the sources, the opacity and multiphase character of the interstellar medium, and the complex morphology of these systems. Over the last several decades, a variety of numerical techniques have been developed to solve the radiative transfer problem with different levels of approximation and in multidimensions. Based on the specific algorithms employed, the approaches can be classified into two general categories: finite-difference and Monte Carlo methods (e.g., Jonsson 2006; see also Pascucci et al. 2004, who describe the codes as "grid-based" or "particle-based" by analogy to hydrodynamic solvers).

Finite-difference codes solve the equations of radiative transfer (RT) iteratively using finite convergence criteria. They either solve the moment equations for RT, originally formulated by Hummer & Rybicki (1971) for spherical geometry with a central point source (e.g., Scoville & Kwan 1976; Leung 1976; Yorke 1980; Wolfire & Cassinelli 1986; Men'shchikov & Henning 1997; Dullemond & Turolla 2000), or employ ray-tracing methods on a discrete spatial grid for complex density configurations (e.g., Rowan-Robinson 1980; Efstathiou & Rowan-Robinson 1990, 1991; Steinacker et al. 2003, 2006; Folini et al. 2003). This technique provides full error control but can be time-consuming.

Monte Carlo methods sample and propagate photons probabilistically (e.g., Witt 1977; Lefevre et al. 1982, 1983; Whitney & Hartmann 1992; Witt et al. 1992; Code & Whitney 1995; Lopez et al. 1995; Lucy 1999; Wolf et al. 1999; Bianchi et al. 2000; Harries 2000; Bjorkman & Wood 2001; Whitney et al. 2003b; Jonsson 2006; Pinte et al. 2006). The Monte Carlo technique is more flexible than the finite-difference one because it tracks the scattering, absorption and reemission of photons (or photon packets) in detail, and can handle arbitrary geometries, but at the cost of computational expense to reduce Poisson noise. However, advances in computing technology and algorithms have made high-accuracy Monte Carlo RT calculations feasible and popular.

In particular, Bjorkman & Wood (2001) have developed a Monte Carlo code to handle radiative equilibrium and temperature corrections, which calculates dust emission self-consistently. It conserves the total photon energy, corrects the frequency distribution of reemitted photons, and requires no iteration as the dust opacity is assumed to be independent of temperature. This code has been used in a number of applications, including protostars that have a disk and an envelope with a single heating source in the center (e.g., Whitney & Hartmann 1992, 1993; Whitney et al. 2003a, 2003b, 2004); circumstellar envelopes (e.g., Wood et al. 1996a, 1996b; Wood et al. 1998); protoplanetary systems (e.g., Wood et al. 2002; Rice et al. 2003); and galaxies that include a bulge and a disk with multiple heating sources from these two populations (e.g., Wood & Jones 1997; Wood & Loeb 2000). This code has also been able to generate optical–far-IR SEDs that reproduce those of a sample of 21 X-ray-selected AGNs (Kuraszkiewicz et al. 2003), and the version of Whitney et al. (2003b) has been applied to simulations of galaxy mergers with black hole feedback to study the properties of local infrared luminous galaxies (Chakrabarti et al. 2007a) and submillimeter galaxies (Chakrabarti et al. 2007b).

In order to produce accurate SEDs of quasars and their hosts formed by galaxy mergers, as in Li et al. (2007) the RT code must satisfy the following requirements: (1) be able to handle arbitrary geometries and distributed heating sources; (2) resolve the large dynamic ranges in spatial scales and densities in the merger simulations; (3) incorporate a multiphase description of the interstellar medium (ISM); and (4) employ a dust model appropriate for a young starburst system.

In many earlier applications, radial logarithmic or uniformly spaced meshes were used to generate density grids. However, in merging galaxies, the ISM is clumpy and irregular owing to shocks and tidal features produced during the interactions, and has multiple density centers, making logarithmic algorithms inefficient. In such a situation, an adaptive grid approach appears ideal for resolving localized high-density regions, while still covering the large volumes of merging systems (Wolf et al. 1999; Kurosawa & Hillier 2001; Harries et al. 2004; Jonsson 2006).

In addition, dust models commonly used in previous works are based on observed extinction curves for the Milky Way (e.g., Weingartner & Draine 2001; Calzetti et al. 1994, 2000; Kim et al.

1994; Mathis et al. 1977), in which the dust is assumed to be produced mainly by old, low-mass stars with ages >1 Gyr (Mathis 1990; Whittet 2003; Dwek 2005). However, a large amount of dust [$\sim(1\text{–}7)\times10^8\ M_\odot$] is detected in the $z \simeq 6.42$ quasar host (Bertoldi et al. 2003a) at a time when the universe was only $\sim$850 Myr old. It has been suggested by observations (e.g., Maiolino et al. 2004, 2006; Moseley et al. 1989; Dunne et al. 2003; Morgan et al. 2003; Sugerman et al. 2006) and theoretical studies (e.g., Todini & Ferrara 2001; Nozawa et al. 2003, 2007; Schneider et al. 2004; Bianchi & Schneider 2007) that supernovae can provide fast and efficient dust formation in the early universe, motivating other choices for the dust model in the RT calculations.

Finally, in a multiphase description of the ISM (McKee & Ostriker 1977), as adopted in our simulations (Springel & Hernquist 2003a; Springel & Hernquist 2003b; Hopkins et al. 2006), the "hot-phase" (diffuse) and "cold-phase" (dense molecular and H I core) components coexist under pressure equilibrium but have different mass fractions and volume filling factors (i.e., the hot-phase gas is $\leq$10% in mass but $\gtrsim$99% in volume), so both phases contribute to the dust extinction and should therefore be included in the RT calculations.

We have refined the Monte Carlo RT code developed by Bjorkman & Wood (2001) and Whitney et al. (2003b) by implementing: an adaptive grid algorithm similar to that of Jonsson (2006) for the density field and the arbitrarily distributed sources; a multiphase ISM model (Springel & Hernquist 2003a), which accounts for observed scaling relations of molecular clouds for the dust distribution; and a supernova-origin dust model for the opacity using the grain size distribution of Todini & Ferrara (2001). We refer to our new code as ART^2 (All-wavelength Radiative Transfer with Adaptive Refinement Tree). ART^2 is capable of producing SEDs and images in a wide range of wavelengths from X-ray to millimeter. In the present paper we focus on the dust properties from optical to submillimeter bands. As we show in what follows, ART^2 reproduces the spectrum of a single galaxy with bulge and disk calculated with the original code. More important, it captures the inhomogeneous density distribution in galaxy mergers and reproduces the observed SED and dust properties of J1148+5251 based on the simulations of Li et al. (2007). Therefore, ART^2 can be used to predict multiwavelength properties of quasar systems and their galaxy progenitors.

This paper is organized as follows. In § 2 we describe our computational methods and models, including the multiscale simulations of Li et al. (2007) for $z \sim 6$ quasar formation, and our implementation of ART^2, which incorporates radiative equilibrium as in Bjorkman & Wood (2001), an adaptive grid, a multiphase ISM, and a supernova-origin dust model. In § 3 we present the multiwavelength SED from optical to submillimeter of a simulated quasar at $z \sim 6.5$. In § 4 we present detailed studies on both the numerical resolutions of the RT calculations and physical parameters of various methods implemented. The dust distribution and properties of the quasar system are presented in § 5, and we describe their evolution in § 6. We discuss the assumptions and robustness of our models in § 7, and summarize in § 8.

2. METHODOLOGY

In order to capture the physical processes underlying the formation and evolution of quasars in the early universe, and to compare their multiwavelength properties to observations, we combine quasar formation and radiative transfer calculations. We first perform a set of novel multiscale simulations that yield a luminous quasar at $z \sim 6.5$ (Li et al. 2007). We then apply the three-dimensional Monte Carlo radiative transfer code, ART^2, to the outputs of the hydrodynamic galaxy mergers simulations to calculate the SED of the system. The models and simulations of quasar formation are described in detail in Li et al. (2007). Here, we briefly summarize the modeling of quasar formation and the specifications of ART^2.

2.1. *Formation Model of $z \sim 6$ Quasars*

2.1.1. *Multiscale Simulations*

The $z \sim 6$ quasars are rare (space density $\sim$1 Gpc^{-3} comoving), and appear to be powered by supermassive black holes of mass $\sim10^9\ M_\odot$. Therefore, simulations of high-redshift quasar formation must consider a large cosmological volume to accommodate the low abundance of this population, have a large dynamic range to follow the hierarchical build-up of the quasar hosts, and include realistic prescriptions for star formation, black hole growth, and associated feedback mechanisms. The multiscale simulations in Li et al. (2007) include both *N*-body cosmological calculations in a volume of 3 Gpc^3 to account for the low number density of quasars at $z \sim 6$, and hydrodynamical simulations of individual galaxy mergers on galactic scales to resolve gas-dynamics, star formation, and black hole growth.

First, we perform a coarse dark matter-only simulation in a volume of 3 Gpc^3. The largest halo at $z = 0$, within which early, luminous quasars are thought to reside (Springel et al. 2005b), is then selected for resimulation at higher resolution. The evolution of this halo and its environment is resimulated using a multigrid zoom-in technique (Gao et al. 2005) that provides much higher mass and spatial resolution for the halo of interest, while following the surrounding large-scale structure at lower resolution. The merging history of the largest halo at $z \sim 6$, which has then reached a mass of $\sim7.7\times10^{12}M_\odot$ through seven major (mass ratio $<5:1$) mergers between redshifts 14.4 and 6.5, is extracted. These major mergers are again resimulated hydrodynamically using galaxy models that include a Hernquist (1990) halo and an exponential disk scaled appropriately for redshift (Robertson et al. 2006), and adjusted to account for mass accretion through minor mergers. Each of these eight galaxy progenitors has a black hole seed assumed to originate from the remnants of the first stars (Abel et al. 2002; Bromm & Larson 2004; Tan & McKee 2004; Yoshida et al. 2003, 2006; Gao et al. 2007).

The simulations were performed using the parallel, *N*-body/smoothed particle hydrodynamics (SPH) code GADGET2 (Springel 2005), which conserves energy and entropy using the variational principle formulation of SPH (Springel & Hernquist 2002), and which incorporates a subresolution model of a multiphase interstellar medium to describe star formation and supernova feedback (Springel & Hernquist 2003a). Star formation is modeled following the Schmidt-Kennicutt law (Schmidt 1959; Kennicutt 1998a). Feedback from supernovae is captured by an effective equation of state for star-forming gas (Springel & Hernquist 2003a). A prescription for supermassive black hole growth and feedback is also included, where black holes are represented by collisionless "sink" particles that interact gravitationally with other components and accrete gas from their surroundings. The accretion rate is estimated from the local gas density and sound speed using a spherical Bondi-Hoyle (Bondi & Hoyle 1944; Bondi 1952) model that is limited by the Eddington rate. Feedback from black hole accretion is modeled as thermal energy injected into the surrounding gas (Springel et al. 2005a; Di Matteo et al. 2005). We note that implementations of our model for black hole growth and feedback that do not explicitly account for Eddington-limited accretion achieve similar results

to the method employed by us (e.g., compare the works of Di Matteo et al. 2008 and Sijacki et al. 2007).

These hydrodynamic simulations adopted the ΛCDM model with cosmological parameters from the first-year *Wilkinson Microwave Anisotropy Probe* data (WMAP1; Spergel et al. 2003), $(\Omega_m, \Omega_b, \Omega_\Lambda, h, n_s, \sigma_8) = (0.3, 0.04, 0.7, 0.7, 1, 0.9)$. In this paper we use the same parameters.

2.1.2. *Hierarchical Assembly of the Quasar System*

In the simulation analyzed here, the quasar host galaxy builds up hierarchically through seven major mergers of gas-rich progenitors between $z = 14.4$–6.5. Gravitational interactions between the merging galaxies form tidal tails, strong shocks and efficient gas inflows that trigger intense starbursts. The highly concentrated gas fuels rapid black hole accretion. Figure 1 shows the evolution of some aspects of the system. In the range $z \sim 14$–9, the merging galaxies are physically small and the interactions occur on scales of tens of kiloparsecs. By $z \sim 9$–7.5, when the last major mergers take place, the interactions have increased dramatically in strength. Galaxies are largely disrupted in close encounters, tidal tails of gas and stars extend over hundreds of kiloparsecs, and powerful bursts of star formation are triggered, resulting in an average star formation rate of $\sim 10^3\ M_\odot\ \mathrm{yr}^{-1}$ that peaks at $z \sim 8.5$. During this phase, the black holes are heavily obscured by circumnuclear gas. The luminosity from the starbursts outshines that from the accreting black holes. So, we refer to this period ($z \sim 14$–7.5) as the "starburst phase."

Once the progenitors have coalesced, the multiple SMBHs from the galaxies merge and grow exponentially in mass and feedback energy via gas accretion. During this period ($z \sim 7.5$–6, hereafter referred to as "quasar phase"), the black hole luminosity outshines that of the stars. At redshift $z \approx 6.5$, when the galaxies coalesce, the induced high central gas densities bring the SMBH accretion and feedback to a climax. The black hole reaches a mass of $\sim 2 \times 10^9\ M_\odot$, and has a peak bolometric luminosity close to that of J1148+5251. Black hole feedback then drives a powerful galactic wind that clears the obscuring material from the center of the system. The SMBH becomes visible briefly as an optically luminous quasar similar to J1148+5251. Once the system relaxes, the SMBH and the host satisfy the relation, $M_{\rm BH} \approx 0.002\ M_{\rm star}$, similar to that measured in nearby galaxies (Magorrian et al. 1998; Marconi & Hunt 2003), as a result of coeval evolution of both components (Li et al. 2007; Robertson et al. 2006; Hopkins et al. 2007c).

After $z < 6$ (the "postquasar phase"), feedback from star formation and the quasar quenches star formation and self-regulates SMBH accretion. Consequently, both star formation and quasar activity decay, leaving behind a remnant which rapidly reddens. The object will eventually evolve into a cD-like galaxy by the present day. (For an overview of this scenario, see, e.g., Hopkins et al. 2007a, 2007b.)

The photometric calculations by Robertson et al. (2007) show that this quasar system satisfies a variety of photometric selection criteria based on Lyman-break techniques. The massive stellar spheroid descended from these $z \sim 6$ quasars could be detected at $z \sim 4$ by existing surveys, while the galaxy progenitors at higher redshifts will likely require future surveys of large portions of the sky ($\gtrsim 0.5\%$) at wavelengths $\lambda \gtrsim 1\ \mu$m owing to their low number densities.

2.2. *ART²: All-Wavelength Radiative Transfer with Adaptive Refinement Tree*

ART² is based on a unification of the three-dimensional Monte Carlo radiative equilibrium code developed by Bjorkman & Wood (2001) and Whitney et al. (2003b), an adaptive grid, a multiphase ISM model, and a supernova-origin dust model. Below, we describe our implementation of ART².

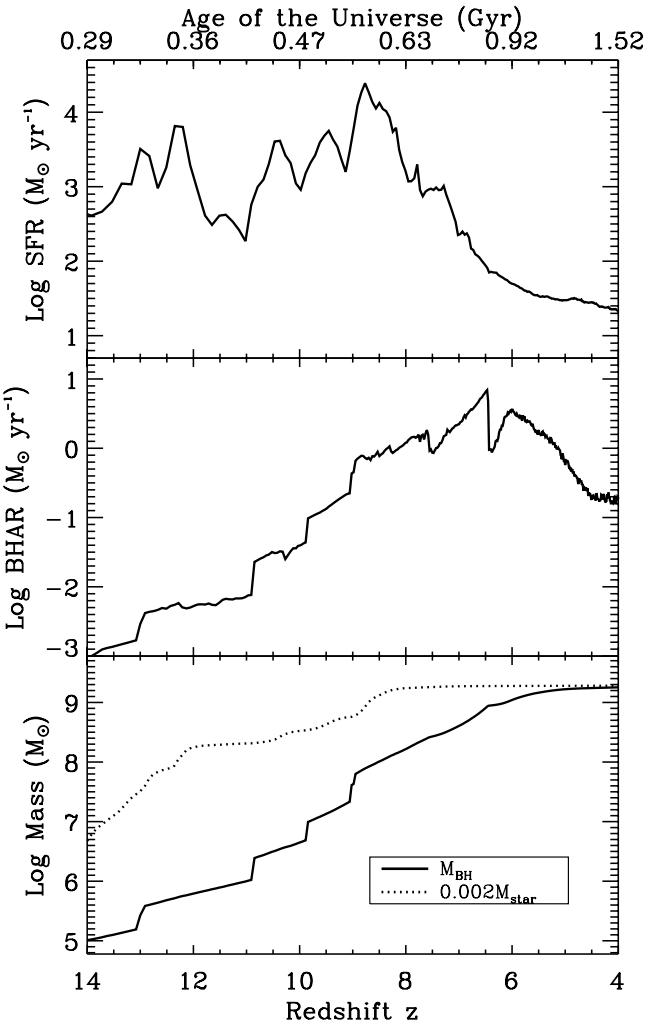

FIG. 1.—Evolution of the star formation rate, black hole accretion rate, and masses of the black holes and stars, respectively, of the simulated quasar system at $z \sim 6.5$, adopted from Li et al. (2007).

2.2.1. *Monte Carlo Radiative Transfer for Dust in Radiative Equilibrium*

The Monte Carlo RT method follows the propagation, scattering, absorption, and reemission of "photon packets" (groups of equal-energy, monochromatic photons that travel in the same direction) by randomly sampling the various probability distribution functions that determine the optical depth, scattering angle, and absorption rates. For the dusty environments we are concerned with, the reemitted spectrum depends on the temperature of the dust, which is assumed to be in thermal equilibrium with the radiation field. In the traditional scheme, the frequencies of the reemitted photons are sampled from local reemission spectra with fixed temperatures. The dust radiative equilibrium is ensured by performing the Monte Carlo transfer iteratively until the dust temperature distribution converges. Such methods often require a large number of iterations and are therefore computationally expensive (Bjorkman & Wood 2001; Pascucci et al. 2004).

Bjorkman & Wood (2001) proposed a solution to this problem by formulating an "immediate reemission" algorithm, in which the dust temperature is immediately updated on absorption of

a photon packet, and the frequencies of reemitted photons are sampled from a spectrum that takes into account the modified temperature. The advantage of this approach is that dust radiative equilibrium and the radiative transfer solutions are obtained simultaneously without iteration. This algorithm is described in detail in Bjorkman & Wood (2001); here we briefly outline the steps.

Assuming that each photon packet carries an energy E_γ, and after absorption of N_i packets in the ith grid cell, the total energy absorbed in the cell is

$$E_i^{\rm abs} = N_i E_\gamma. \quad (1)$$

In radiative equilibrium, this energy must be reradiated, with a thermal emissivity of $j_\nu = \kappa_\nu \rho B_\nu(T)$, where κ_ν is the absorptive opacity, ρ is the dust density, and $B_\nu(T)$ is the Planck function at temperature T,

$$B_\nu(T) = \frac{2h_{\rm P}}{c^2} \frac{\nu^3}{e^{h_{\rm P}\nu/(kT)} - 1}, \quad (2)$$

where $h_{\rm P}$ is Planck's constant, c is the speed of light, and k is Boltzmann's constant. The emitted energy in the time interval Δt is

$$E_i^{\rm em} = 4\pi\Delta t \int dV_i \int \rho\kappa_\nu B_\nu(T)\, d\nu = 4\pi\Delta t \kappa_{\rm P}(T_i) B(T_i) m_i, \quad (3)$$

where $\kappa_{\rm P} = \int \kappa_\nu B_\nu d\nu / B$ is the Planck mean opacity, $B = \sigma T^4/\pi$ is the frequency integrated Planck function, and m_i is the dust mass in the cell.

Equating the absorbed (1) and emitted (3) energies, we obtain the dust temperature as follows after absorbing N_i packets:

$$\sigma T_i^4 = \frac{N_i L}{4 N_\gamma \kappa_{\rm P}(T_i) m_i}, \quad (4)$$

where N_γ is the total number of photon packets in the simulation, and L is the total source luminosity. Note that because the dust opacity is temperature-independent, the product $\kappa_{\rm P}(T_i)\sigma T_i^4$ increases monotonically with temperature. Consequently, T_i always increases when the cell absorbs an additional packet.

The added energy to be radiated owing to the temperature increase ΔT is determined by a temperature-corrected emissivity Δj_ν in the following approximation when the temperature increase, ΔT, is small:

$$\Delta j_\nu \approx \kappa_\nu \rho \Delta T \frac{dB_\nu(T)}{dT}. \quad (5)$$

The reemitted packets, which comprise the diffuse radiation field, then continue to be scattered, absorbed, and reemitted until they finally escape from the system. This method conserves the total energy exactly, and does not require any iteration as the emergent SED, $\nu L_\nu = \kappa_\nu B_\nu(T)$, corresponds to the equilibrium temperature distribution (Bjorkman & Wood 2001).

This Monte Carlo radiative equilibrium code works as follows: first, the photon packets are followed to random interaction locations, determined by the optical depth. Then they are either scattered or absorbed with a probability given by the albedo ($a = n_s\sigma_s/n_s\sigma_s + n_a\sigma_a$, where n and σ are number density and cross section for either scattering or absorption, respectively). If the packet is scattered, a random scattering angle is obtained from the scattering phase function. If instead the packet is absorbed, it is reemitted immediately at a new frequency determined by the envelope temperature, using the algorithm described above. After either scattering or absorption plus reemission, the photon packet continues to a new interaction location. This process is repeated until all the packets escape the dusty environment. On completion of the Monte Carlo transfer, the code produces emergent SEDs and images at any given inclination for a wide range of broadband filters, including those of *Hubble Space Telescope* (NICMOS bands), *Spitzer* (IRAC and MIPS bands), and *SCUBA* submillimeter bands.

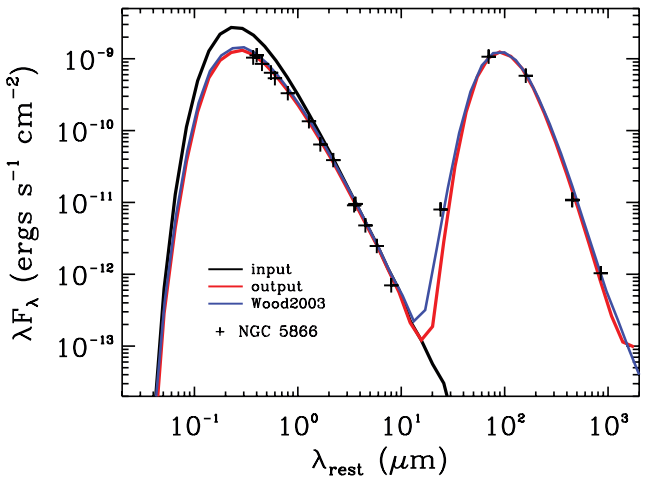

FIG. 2.—Test run of the radiative equilibrium algorithm adopted from Bjorkman & Wood (2001) on three-dimensional Cartesian coordinates for a simple galaxy with a bulge and a disk. The input spectrum of the stars is a blackbody with a temperature of 15000 K (*black curve*). The red curve is our output, the blue curve is simulation data from K. Wood, and the crosses are observations of a lenticular galaxy NGC 5866, which has an unusual extended dust disk seen exactly edge-on. Both Wood's data and the observations come with the code release package from K. Wood (http://www-star.st-and.ac.uk/~kw25/research/montecarlo/gals/gals.html).

Bjorkman & Wood (2001) tested this algorithm extensively by comparing a set of benchmark calculations to those of Ivezić et al. (1997) for spherical geometry. Baes et al. (2005) critically study the frequency distribution adjustment used by Bjorkman & Wood (2001) and give a firm theoretical basis for their method, although it may fail for small dust grains.

One drawback of this code, however, is its fixed geometry and limited dynamic range. It can handle only two- or three-dimensional spherical-polar grids, which are not suitable for capturing the arbitrary geometry and large dynamic ranges characteristic of merging galaxies, which have multiple density centers, and where gas and stars extend hundreds of kiloparsecs and shocks produce highly condensed gas on scales of parsecs. We have developed an improved version of this code by implementing an adaptive Cartesian grid on top of the code released by Wood.[5]

To ensure that our implementation of the algorithm is correct, we rerun the test problem that comes with the code release package of Wood using a uniform Cartesian grid. The test problem consists of a simple galaxy with bulge and disk components. As is shown in Figure 2, our code reproduces the result of Wood very well.

2.2.2. *Adaptive-Mesh Refinement Grid*

The SPH simulations using GADGET2 (Springel 2005) output hydrodynamic information as particle data. However, the ray

[5] See http://www-star.st-and.ac.uk/~kw25/research/montecarlo/gals/gals.html.

tracing in the RT calculation is done on a grid. Therefore, it is necessary to interpolate the particle-based density field onto a grid. Jonsson (2006) performed radiative transfer calculations on SPH simulations of galaxy mergers using an adaptive grid as implemented in his Monte Carlo RT code, SUNRISE. Unfortunately, self-consistent calculations of dust radiative equilibrium and emission are not yet included in SUNRISE.

Our algorithm for constructing adaptive grids is similar to that of Jonsson (2006). We typically start with a base grid of a 4^3 box covering the entire simulation volume. Each cell is then adaptively refined by dividing it into 2^3 subcells. The refinement is stopped if a predefined maximum refinement level, RL, is reached, or if the total number of particles in the cell becomes less than a certain threshold, whichever criterion is satisfied first. The maximum refinement level used in the present work is 12, and the maximum particle number allowed in the cell is 32, half the number of the SPH smoothing kernel neighbors used in the GADGET2 simulations. The resolution of the finest level is therefore $L_{\rm min} = L_{\rm box}/2^{({\rm RL}+1)}$, where $L_{\rm box}$ is the box length, and RL is again the maximum refinement level. For example, for the parameters used in this simulation, $L_{\rm box} = 200$ kpc, RL $= 12$, we have $L_{\rm min} = 24.4$ pc.

The adaptive-mesh refinement grid serves as an efficient tree for mass assignment owing to fast neighbor finding within the grids for SPH smoothing. After the grid is constructed, the gas properties at the center of each grid cell, such as density, temperature, and metallicity, are calculated using the SPH smoothing kernel (Hernquist & Katz 1989) of the original simulation. All physical quantities are assumed to be uniform across a single cell.

Figure 3 gives an example of the adaptive grid applied to a snapshot from the galaxy merger simulations in Li et al. (2007) and compared with a uniform grid. This particular snapshot represents the time when the system reaches the peak quasar phase, when the galaxies are in the final stages of coalescence. The system is highly dynamical as much gas is falling into the center, while feedback from the central massive black hole drives an outflow. The gas distribution is thus inhomogeneous.

As is apparent in Figure 3, a uniform grid of 50^3 (*top*) barely captures the density distribution with a spatial resolution of 4 kpc. The resolution is worse than an adaptive grid with a moderate maximum refinement level (i.e., RL $= 5$, *middle panel*), which has a finest cell length of $\sim$3.1 kpc. The grid with a maximum refinement level of 12 shown in the bottom panel fully captures the large dynamic range of the gas density distribution in three dimensions. It has a minimum cell length of $\sim$24.4 pc for the finest cells, which is comparable to the spatial resolution of the original hydrodynamic simulation of Li et al. (2007). This resolution is equivalent to a $\sim 10{,}000^3$ uniform grid, which is impractical with existing computational facilities.

2.2.3. *A Multiphase Model for the Interstellar Medium*

In determining the dust distribution, we adopt the multiphase model of Springel & Hernquist (2003a) for the ISM. The ISM is then comprised of condensed clouds in pressure equilibrium with an ambient hot gas, as in the picture of McKee & Ostriker (1977). In the hydrodynamic simulations, individual SPH particles represent regions of gas that contain cold, dense cores embedded in a hot, diffuse medium. The hot and cold phases of the ISM coexist in pressure equilibrium but have different mass fractions and volume filling factors (i.e., the hot-phase gas is $\leq$10% in mass but $\gtrsim$99% in volume). In our previous studies, Li et al. (2007) and Hopkins et al. (2006) used only the hot-phase density to determine e.g., the obscuration of the central AGN, as the majority of sight lines will pass through only this component owing to its large volume filling factor. However, this method gives only an effective lower limit on the column density.

Here, we consider two components of the dust distribution, having different dust-to-gas ratios and being associated with the two phases of the ISM. Within each grid cell in the RT calculation, the hot gas is uniformly distributed, while the cold, dense cores are randomly embedded. Because of the much higher density and smaller volume of the cold phase, it is impractical to resolve these clouds either in hydrodynamic simulations or in our radiative transfer calculations. Consequently, we implement an observationally-motivated, subresolution prescription to treat the cold clouds, constrained by the observed mass spectrum and size distribution of molecular clouds in galaxies.

Observations of giant molecular clouds (GMCs) in galaxies show that the GMCs follow simple scaling relations (Larson 1981), namely, a power-law mass distribution, $dN/dM \propto M^{-2}$ (e.g., Fuller & Myers 1992; Ward-Thompson et al. 1994; Andre et al. 1996; Blitz & Rosolowsky 2006), as well as a power-law mass-radius relation $M \propto R^2$ (e.g., Sanders et al. 1985; Dame et al. 1986; Scoville et al. 1987; Solomon et al. 1987; Rosolowsky 2005, 2007). It has been suggested by theoretical modeling that the mass function is produced by turbulence in self-gravitating clouds (e.g., Elmegreen & Falgarone 1996; Elmegreen 2002; Ballesteros-Paredes & Mac Low 2002; Li et al. 2003), while the mass-radius relation is attributed to virial equilibrium (Larson 1981).

Here we incorporate these two empirical relations into our ISM model for the RT calculations. For a given cell, the two-phase break-down in Springel & Hernquist (2003a) determines the hot and cold phase gas density according to pressure equilibrium. The cold clouds are assumed to follow the Larson scaling relations:

$$\frac{dn}{dM} = AM^{-\alpha}, \tag{6}$$

$$M = BR^{\beta}, \tag{7}$$

where dn/dM is the number density of the clouds differential in cloud mass M, and R is the cloud radius. From these equations, one obtains the cloud size distribution

$$\frac{dn}{dR} = \beta AB^{1-\alpha} R^{-(\alpha\beta+1-\beta)} = CR^{-\gamma}, \tag{8}$$

where $C = \beta AB^{1-\alpha}$ and $\gamma = \alpha\beta + 1 - \beta$.

Assume that the minimum and maximum values of the cloud mass are M_0 and M_1, then the normalization constant of the mass spectrum for each cell can be determined using

$$\int \frac{dn}{dM} M\, dM = x_c \rho_c, \tag{9}$$

or

$$A = x_c \rho_c \frac{2-\alpha}{M_1^{2-\alpha} - M_0^{2-\alpha}}, \tag{10}$$

where ρ_c and x_c are the cold gas density and volume filling factor, respectively. The normalization constant of the M-R relation may be determined using

$$x_c = \int \frac{4\pi}{3} R^3 \frac{dn}{dM}\, dM, \tag{11}$$

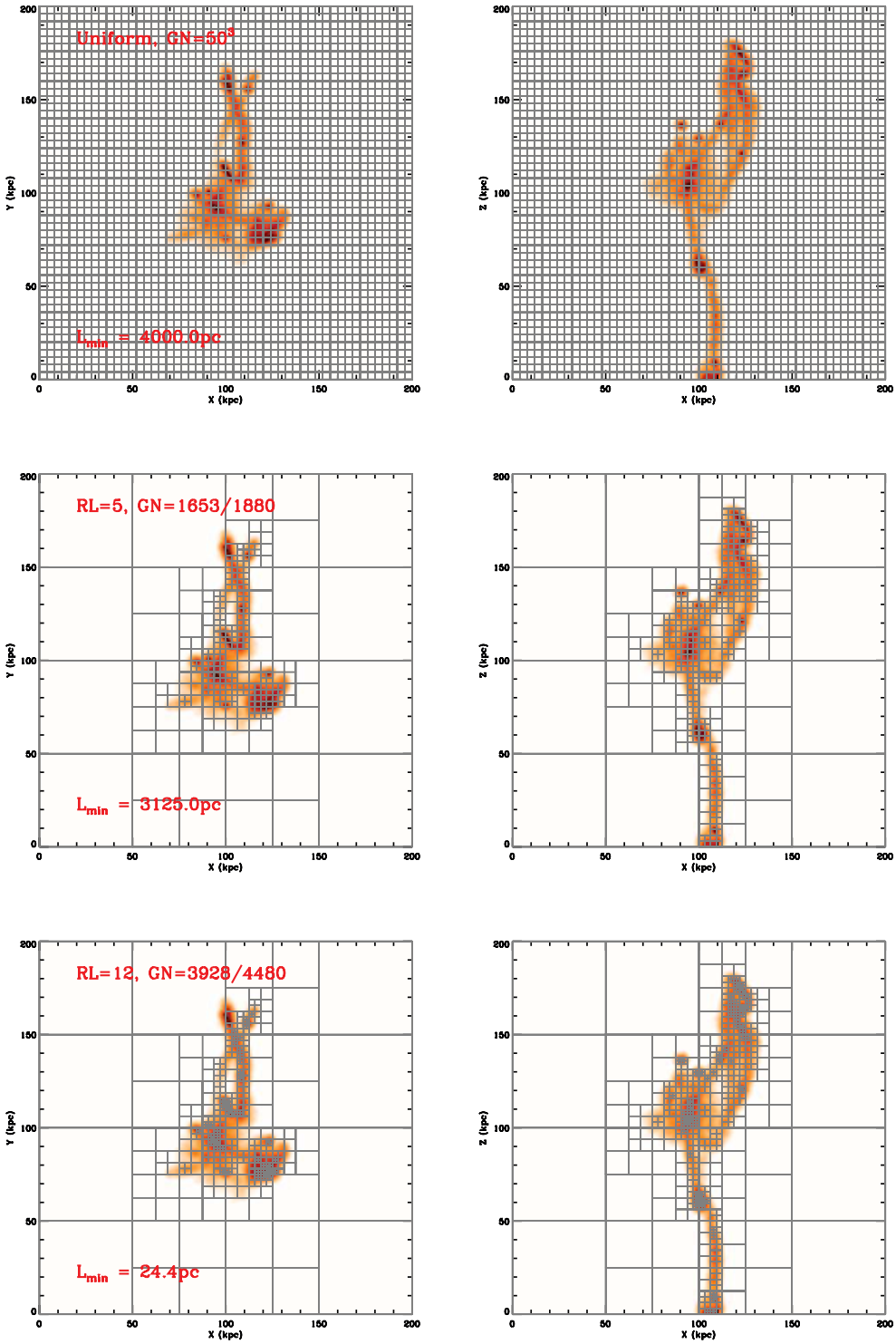

FIG. 3.— Example of the adaptive grid applied to a snapshot of the galaxy merger from Li et al. (2007). From top to bottom is: uniform grid, and adaptive grids with maximum refinement levels of RL = 5 and 12, respectively. The label GN indicates the total grid number covering the entire volume (in case of adaptive grids, it provides the number of the finest grid and that of the total grid). This plot demonstrates that adaptive grids with sufficient refinement capture the density distribution well, while the uniform grid fails to do so unless an unreasonably large number of cells is employed. Throughout this paper, we use a maximum refinement level of 12, which has a grid resolution comparable to that of the hydrodynamic simulations in Li et al. (2007).

or

$$B = \left[\frac{4\pi A}{3\eta x_c}\left(M_1^{\eta} - M_0^{\eta}\right)\right]^{\beta/3}, \quad (12)$$

where

$$\eta = 1 + \frac{3}{\beta} - \alpha. \quad (13)$$

The minimum and maximum cloud radii in the cell are therefore

$$R_0 = \left(\frac{M_0}{B}\right)^{1/\beta}, \quad R_1 = \left(\frac{M_1}{B}\right)^{1/\beta}. \quad (14)$$

For a photon traveling a distance L in the cell, the average number of cold clouds of radius R the photon will intersect is given by

$$\frac{dN}{dR} = \pi R^2 L \frac{dn}{dR} = \pi C R^{2-\gamma}. \quad (15)$$

Integrating over the cloud radius, one obtains

$$N = \pi L C \frac{R_1^{3-\gamma} - R_0^{3-\gamma}}{3-\gamma}. \quad (16)$$

Therefore, the average distance the photon must travel to hit a cold cloud (the mean free path) is given by

$$L_m = \frac{3-\gamma}{\pi C\left(R_1^{3-\gamma} - R_0^{3-\gamma}\right)}. \quad (17)$$

In the dust RT calculation, we assume that dust is associated with both the cold and hot phase gases through certain dust-to-gas ratios. When a photon enters a cell, we first determine the distance L_H it travels in the hot phase gas before hitting a cold cloud, which is an exponential distribution function

$$p(L) = \frac{1}{L_m}\exp\left(-\frac{L}{L_m}\right). \quad (18)$$

Therefore, $L_h = -L_m \ln \xi$, where ξ is a random number uniformly distributed between 0 and 1. The radius of the cloud the photon just hits is also determined randomly assuming the distribution function of equation (15); i.e.,

$$R = \left[R_0^{3-\gamma} + \left(R_1^{3-\gamma} - R_0^{3-\gamma}\right)\xi\right]^{1/(3-\gamma)}. \quad (19)$$

The distance L_c the photon travels in this cold cloud is again a random variable given by $L_c = 2R\sqrt{\xi}$, because clouds are assumed to be uniformly distributed. These equations completely define the statistical procedure for determining the dust column densities associated with L_h and L_c as

$$N_h = \rho_h L_h, \quad N_c = \frac{3BR^{\beta-3}L_c}{4\pi}. \quad (20)$$

With a given dust opacity curve, these equations allow one to calculate the optical depths, τ_h and τ_c for the hot and cold dust, respectively. They relate the photon path lengths in the multiphase ISM to the total optical depth $\tau_{\rm tot}$, which is then compared with a randomly drawn number τ_i, to determine whether the photon should be stopped for scattering or absorption. In detail, the Monte Carlo ray-tracing procedure for the radiative transfer therefore involves the following steps:

1. A photon packet is emitted from either a black hole or a stellar source with random frequencies consistent with the source spectra. The photon is emitted with a uniformly distributed random direction. The probability of a photon being emitted by any given source is determined by its luminosity relative to the total.
2. A random optical depth over which the photon must travel before an interaction with the dust occurs, $\tau_i = -\ln \xi$, is drawn to determine the interaction location. The interaction includes scattering and absorption. In our method, the photon energies are not weighted, only one event is allowed. That is, at any given interaction site, the photon is either scattered or absorbed, but not both.
3. Starting from the location of the photon emission, the cumulative optical depth of the photon, $\tau_{\rm tot}$, is calculated stochastically using equation (20) for both hot and cold dusts. If the photon is stopped for interaction within a single cell, then $\tau_{\rm tot}$ is the sum of contributions from possibly multiple segments of both hot and cold dusts within this cell. If the photon passes through multiple cells before an interaction occurs, then $\tau_{\rm tot}$ is the sum of all contributions from relevant segments in these cells.
4. At each boundary between the hot and cold phase gas clouds, or at the boundary of the grid cell, the next interaction point is determined by the comparison between τ_i and $\tau_{\rm tot}$. If $\tau_i \leq \tau_{\rm tot}$, then the photon is either scattered or absorbed, with a probability given by the scattering albedo. The exact interaction location is then determined inside either hot or cold phase gas, such that $\tau_{\rm tot}$ becomes exactly τ_i. If the photon is scattered, its direction and polarization state are altered using the Henyey-Greenstein phase function, and the ray tracing of the new photon is repeated from step 2. If the photon is absorbed, depending on whether the absorption site occurs in the hot or cold phase dust, the temperature of the appropriate dust cell is raised, and a new photon is reemitted according to the scheme of Bjorkman & Wood (2001). The ray tracing of the newly emitted photon again restarts from step 2.
5. If the photon escapes from the system without reaching the optical depth τ_i, it is then collected in the output spectrum and image. The next photon will be picked up from the source, and the whole Monte Carlo procedure from step 1 will be restarted.

After all N_γ photons have been traced, one obtains the dust temperature distribution for both hot and cold dusts in radiative equilibrium, as well as the output spectra and images. Note that such a stochastic procedure outlined here may not be as accurate as physically tracking the locations and sizes of the cold-phase gas clouds, which can be rather difficult, if not impossible. However, this method works efficiently for a large number of cold clouds uniformly distributed in the cells, and it gives correct average extinction properties for a multiphase ISM model we are interested here.

Hereafter, we refer to "HPG dust" as the dust that originates from the hot-phase gas, and "CPG dust" as that originating from the cold-phase gas. Note that the gas only determines the distribution and mass of the dust through a given dust-to-gas ratio. The dust temperature is not associated with the gas temperature, and is calculated self-consistently according to radiative equilibrium. We further refer to "cold dust," "warm dust," and "hot dust" as dust with temperatures $T \lesssim 100$ K, $100 \lesssim T \lesssim 1000$ K, and $1000 \lesssim T \lesssim 1200$ K, respectively.

In the RT calculations, we adopt a mass spectrum with $\alpha = 1.8$, as suggested by the observations of Blitz & Rosolowsky (2006) and an observed mass-radius relation with $\beta = 2.0$, which is also a result of the virial theorem. The resulting mass-radius relation in our simulations has a normalization in the range ~ 10–$10^4\ M_\odot\ \mathrm{pc}^{-2}$. For a cloud size of ~ 1 pc, the normalization is $\sim 300\ M_\odot\ \mathrm{pc}^{-2}$, similar to observations of the Milky Way (Scoville et al. 1987; Rosolowsky 2007). It has been shown that the normalization of the mass-radius relationship depends on galactic environment (e.g., Elmegreen 1989; Rosolowsky 2005; Blitz et al. 2007). For example, it is about $\sim 50\ M_\odot\ \mathrm{pc}^{-2}$ in the Large Magellanic Cloud but could be 2 orders of magnitude higher in ULIRGs. In extreme starburst galaxies, the normalization could go up to $10^4\ M_\odot\ \mathrm{pc}^{-2}$, as we find in our simulations.

We assume the cold clouds to be in the mass range of $M_0 = 10^3\ M_\odot$ and $M_1 = 10^7\ M_\odot$, which is similar to that of protoclusters clouds in star forming galaxies, as shown in Li et al. (2004, 2005a, 2005b, 2006). For the cold clouds, we have enhanced the pressure by a factor of 10 over the thermal pressure to account for the effects of turbulence (e.g., Blitz & Rosolowsky 2006; Chakrabarti et al. 2007a). This enhancement factor is referred to as "CP" hereafter. The dust-to-gas ratio of the cold clouds is chosen to be the same as the Milky Way value (1 : 124; Weingartner & Draine 2001), as found in a large sample of ULIRGs (Dunne & Eales 2001; Klaas et al. 2001), while that of the hot, diffuse gas is chosen to be 1% of the Milky Way value, consistent with the dust survival rate of sputtering in a hot, diffuse ISM (Burke & Silk 1974; Reynolds et al. 1997). Observations of some obscured or red AGNs also suggest a ratio significantly lower than that of Milky Way (e.g., Maiolino et al. 2001; Kuraszkiewicz et al. 2003; Hall et al. 2006). We will perform a systematic parameter study of these choices in § 4. However, we note that these values are found to best reproduce the observed quasar SED at $z \sim 6.5$. Because the dust opacity is proportional to the gas metallicity, the dust opacity is weighted by the metallicity of the gas for both hot and cold gas phases.

2.2.4. *Supernova-Origin Dust Model*

Our understanding of the formation and distribution of dust has benefited from dust maps of the Milky Way (e.g., Gehrz 1989; Schlegel et al. 1998). In particular, Gehrz (1989) concludes from a detailed Galactic survey of dust-producing stars that dust in the Milky Way originates in three principle ways: (1) by condensation in winds of evolved, post–main-sequence objects, which accounts of ~90% of the stellar dust; (2) by condensation in ejecta from massive novae, supernovae and Wolf-Rayet stars, which amounts to <10%; and (3) by slow accretion in molecular clouds (see also Marchenko 2006 for a review).

Over the past several decades, various dust models have been developed based on the observed extinction curves of the Large Magellanic Cloud (LMC), the Small Magellanic Cloud (SMC), and the Milky Way (e.g., see reviews by Savage & Mathis 1979; Mathis 1990; Calzetti et al. 1994,2000; Dorschner & Henning 1995; Whittet 2003; Draine 2003). In these classical models, dust is assumed to form in the envelopes of old, low-mass stars such as asymptotic giant branch (AGB) stars with ages $\gtrsim 1$ Gyrs (Mathis 1990; Morgan & Edmunds 2003; Dwek 2005; Marchenko 2006).

However, this picture may be different for young, high-redshift objects. Recent deep millimeter and submillimeter observations of several $z \sim 6$ quasars, which trace the far-infrared thermal dust emission from these systems, show large masses of dust in these quasar hosts when the universe was less than 1 Gyr old (e.g., Bertoldi et al. 2003a; Charmandaris et al. 2004; Robson et al. 2004; Carilli et al. 2004; Maiolino et al. 2004; Beelen et al. 2006; Hines et al. 2006; Jiang et al. 2006; Willott et al. 2007). In particular, Maiolino et al. (2004) find that the extinction curve of the reddened quasar SDSS J1048+46 at $z = 6.2$ is different from those observed at $z < 4$ (similar to that of the Small Magellanic Cloud, Hopkins et al. 2004), but matches the extinction curve expected for dust produced by supernovae.

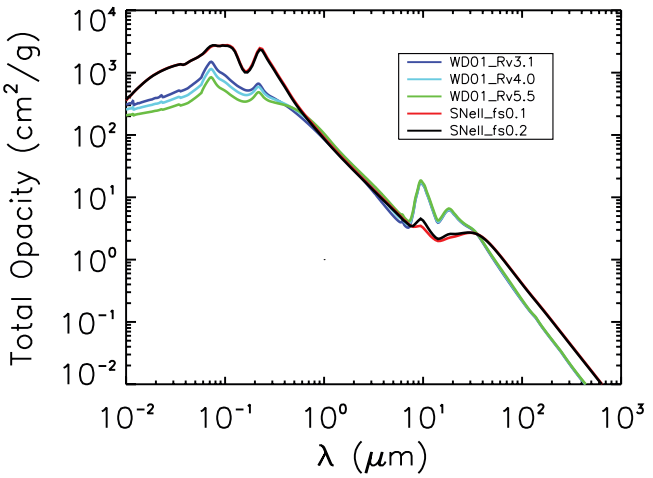

FIG. 4.—Comparison of the dust absorption opacity curves from a supernova-origin dust model (SN model, with silicate fraction $f_s = 10\%$, 20% in red and black, respectively) and those of Weingartner & Draine (2001) (WD01 model, with $R_V = 3.1$, 4.0, 5.5, in blue, cyan, and green, respectively). Note there are two differences between these two models: the silicate feature at ~9.7 μm, and a higher opacity in the optical band.

It has been suggested that core-collapse supernovae (Type II SNe) may provide a fast and efficient mechanism for dust production. The observational evidence for dust formation in SNe comes from observations of SN 1987A (e.g., Gehrz & Ney 1987; Moseley et al. 1989; Roche et al. 1993; Spyromilio et al. 1993; Colgan et al. 1994), Cassiopeia A (Dunne et al. 2003; Dwek 2004; see however Krause et al. 2004, who argue that the dust emission is not associated with the remnant), Kepler's supernova remnant (Morgan et al. 2003), and SN 2003gd (Sugerman et al. 2006). Theoretically, several groups have calculated dust formation in the ejecta of Type II SNe (Todini & Ferrara 2001; Nozawa et al. 2003; Schneider et al. 2004; Hirashita et al. 2005; Dwek et al. 2007). In particular, Todini & Ferrara (2001) have developed a dust model based on standard nucleation theory and tested it on the well-studied case of SN1987A. They find that SNe with masses in the range of 12–35 $M_\odot$ produce about 1% of the mass in dust per supernova for primordial metallicity, and ~3% for solar metallicity.

In the present work, we adopt the dust size distribution of Todini & Ferrara (2001) for solar metallicity and a $M = 22\ M_\odot$ SN model, as in Figure 5 in their paper. This size distribution is then combined with the dust absorption and scattering cross sections of Weingartner & Draine (2001) to calculate dust absorption opacity curves (Finkbeiner 1999; Finkbeiner et al. 1999). We note that Bianchi & Schneider (2007) reanalyze the model of Todini & Ferrara (2001) and follow the evolution of newly condensed grains from the time of formation to their survival. This new feature shows better agreement with observations and further supports our motivation to use a SN dust model. Figure 4 shows dust absorption opacity curves, in the range 10^{-2} to 10^4 μm, from both the supernova-origin dust model (hereafter SN model) and Weingartner & Draine (2001) (hereafter WD model), respectively. The SN models include silicate fractions $f_s = 10\%$ (*red*) and $f_s = 20\%$ (*black*), which show slight differences in

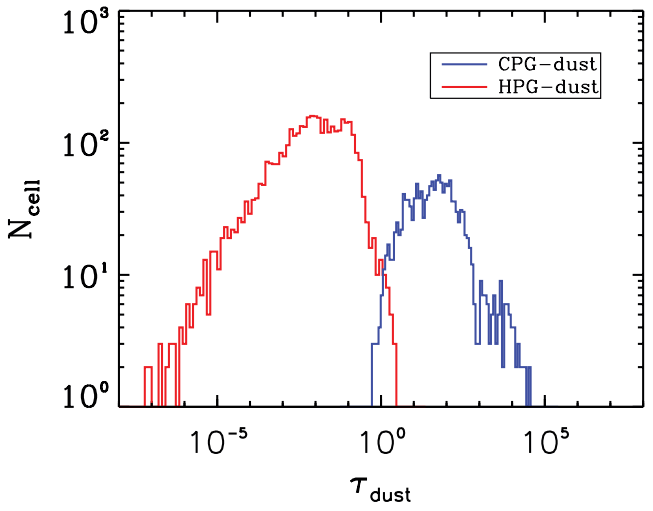

FIG. 5.—Distribution of the optical depths of both HPG and CPG dust, respectively, at $\lambda = 0.1$ μm, where the dust opacity peaks as shown in Fig. 4. The density grid corresponds to the simulation snapshot at $z = 6.5$ shown in Fig. 3 (*bottom*). The "HPG dust" and "CPG dust" refer to the dust associated with hot-phase and cold-phase gas, respectively, as described in § 2.2.3.

the silicate feature at ~9.7 μm ($f_s = 20\%$ model has a slightly higher opacity). The WD models include all the curves commonly used with extinction $R_V = A(V)/[A(B) - A(V) = 3.1]$, 4.0, 5.5, which differ in the opacity in the UV-NIR (0.01–1 μm) bands ($R_V = 3.1$ model has the highest opacity).

Between the SN and WD models, there are two noticeable differences; one is the silicate feature at ~9.7 μm, and the second is the UV-NIR band. On one hand, the WD model has strong peaks around ~9.7 μm (silicate feature), while the SN model produces an opacity lower by nearly 1 order of magnitude, because the ejecta of SNe with mass above 15 $M_\odot$ predominantly form amorphous carbon grains, which decreases the silicate fraction in the dust grains. On the other hand, the SN model increases the opacity in the optical band by a factor of a few owing to the smaller grain size. We note that the small grain sizes may cause quantum fluctuations in the temperature and high-temperature transients (e.g., Draine & Li 2001). However, the dust produced by the SN model is dominated by graphite grains, which have a size distribution from ~100–2000 Å, comparable to the size range of the dust grains in the WD model, so the temperature fluctuation is expected to be insignificant. Note we do not include polycyclic aromatic hydrocarbon (PAH) features at ~7.7 μm, which was modeled in detail by Li & Draine (2002) and Draine & Li (2007). The PAH feature is a good diagnostic of starbursts at low redshifts (Houck et al. 2005); however, it is very difficult to detect in $z \gtrsim 6$ systems. Also, dust spin is not included in our modeling, which could be significant around 10 mm (Draine & Lazarian 1998; Finkbeiner et al. 2002).

The differences between these two models, in particular the silicate feature, may be diminished by choosing different grain compositions and size distributions (Laor & Draine 1993). For example, the WD model would converge to the SN model if the silicate fraction is reduced to ~5%. We note that Elvis et al. (2002) propose an alternative mechanism for dust production in quasars. They suggest that the physical conditions (i.e., low temperature and high density) in the quasar outflow are similar to those in the envelopes of AGB stars, and hence may produce dust similar to that made by AGB stars. This scenario does not have the same timescale issue as does the AGB model, but only requires heavy metals such as carbon and silicate, which should be available

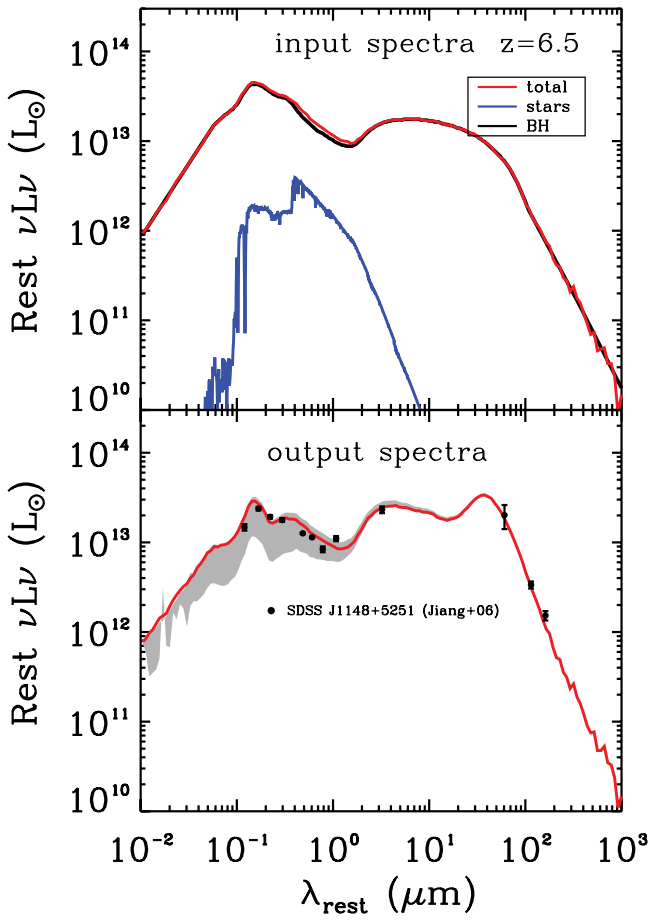

FIG. 6.—SEDs of a quasar system at $z \simeq 6.5$ determined by applying ART^2 to the SPH simulations of Li et al. (2007). The input spectra (*top*) include the stellar spectrum (*blue*) calculated with STARBURST99 (Leitherer et al. 1999; Vázquez & Leitherer 2005), and the composite spectrum of the AGN (Hopkins et al. 2007d; *black*). Note this snapshot corresponds to the peak quasar phase of the system, the stellar radiation is insignificant compared to that from the AGN at this evolution stage. The red curve is the total input spectrum. The output spectra are shown in the bottom panel. The red curve is the total SED assuming an isotropic distribution of photon energies in all directions, while the gray region indicates the range from two orthogonal angles corresponding to the z-axis and (x-y)-plane of the Cartesian grid, respectively. The filled black circles with error bars are observations from Jiang et al. (2006).

even in high-redshift quasars, as noted in the introduction. Therefore, quasar winds may also serve as efficient factories for producing dust with extinction curves similar to those of the WD model. Currently there are no observations available to distinguish between these models at high redshifts. We will return to this in § 4.4.

Figure 5 shows an example of the resulting optical depths of both HPG and CPG dust at wavelength $\lambda = 0.1$ μm where the dust opacity reaches its maximum, as shown in Figure 4. This plot demonstrates that the optical depth is resolved very well in the hot, diffuse gas which occupies ~99% of the volume, while the optical depth of the cold, dense cores is usually much larger than unity, in particular in optical bands with high frequencies. The energy absorbed by the cold dust in these wavelengths is then reemitted at infrared or longer wavelengths.

3. THE SPECTRAL ENERGY DISTRIBUTION OF A QUASAR SYSTEM AT $z \simeq 6.5$

We now calculate the spectral energy distribution from UV/optical to submillimeter of the modeled quasar in Li et al. (2007)

by applying ART^2 to our SPH simulations, which provide the gas density field and heating sources for the RT calculations. The input spectrum includes that from stars and black holes, as shown in Figure 6 (*top panel*). The stellar spectrum is calculated using the stellar population synthesis code STARBURST99 (Leitherer et al. 1999; Vázquez & Leitherer 2005). The age, mass, and metallicity of the stars are taken from the SPH simulations of quasar formation in Li et al. (2007), while the stellar initial mass function (IMF) is assumed to be a top-heavy Kroupa IMF (Kroupa 2002), which characterizes a starburst better than the classical Salpeter IMF (Salpeter 1955).

The input black hole spectrum is a composite template from Hopkins et al. (2007d), which consists of a broken power law (e.g., Laor & Draine 1993; Marconi et al. 2004) and an IR component thought to come from the hottest dust around the AGN, which cannot be fully resolved in our hydrodynamic simulations. The normalization of this spectrum is the total bolometric luminosity of the black holes. Compared to the luminosity calculation in Li et al. (2007), the black hole spectrum here is normalized to the bolometric luminosity of J1148+5251. Heating by cosmic microwave background radiation at different redshifts z is also taken into account by including a uniform radiation field with temperature of $T_{\rm CMB} = 2.73 \times (1 + z)$ K.

The emergent spectrum has a wavelength range of $10^2 - 2 \times 10^7$ Å in the rest frame, and 50 viewing angles (10 in polar angle evenly divided in $\cos\theta$ and 5 in azimuthal ϕ). We use 10^7 photon packets isotropically emitted from sources, and the maximum refinement level of the adaptive grid is RL = 12, which is above the requirement for convergence (see § 4.1 for resolution studies).

The calculated rest-frame SEDs of the system during the peak quasar phase at $z = 6.5$ are shown in Figure 6 (*bottom panel*). The output SED depends on the viewing angle. The red curve is the isotropically averaged SED (e.g., it can be understood as an average SED multiplied by the solid angle 4π). This averaged SED agrees very well with observations of J1148+5251 (Jiang et al. 2006). A prominent feature of this SED is the two infrared bumps peaking around 3 and 50 μm. The 50 μm bump is produced by cold dust ($T \sim 50$ K) heated by strong star formation, as commonly seen in the SEDs of starburst galaxies (Sanders & Mirabel 1996; Siebenmorgen & Krügel 2007). The 3 μm bump is produced by the hot dust ($T \sim 1000$ K) heated by the central AGN. This unique feature appears to be ubiquitous in most of the quasar SEDs over a wide range of redshifts (e.g., Elvis et al. 1994; Vanden Berk et al. 2001; Telfer et al. 2002; Vignali et al. 2003; Richards et al. 2006; Jiang et al. 2006).

To demonstrate the line-of-sight dependence, Figure 6 also shows the range of SEDs viewed from two orthogonal angles of the Cartesian grid: along the z-axis (upper range) and the (x, y)-plane (lower range), respectively. This range indicates difference in column density along the sight lines, and shows that dust extinction in the UV/optical bands differs by a factor of $\sim$3, but no difference at wavelengths longward of 1 μm. This suggests that the dust is close to optically thin along these two viewing angles during this time, and that infrared or submillimeter observations of luminous quasars may not be diagnostics for the orientation of the host. We have also checked the three major components of the output SED, namely, the scatter, escape, and reemission, and found that the photon energy is conserved. This confirms the photon conservation algorithm used in the radiative transfer calculation. Moreover, we find that the emergent SED in the UV/optical bands (0.01–1 μm) is dominated by scattering.

It is interesting to comment on the spectral feature at wavelength $\lambda_{\rm rest} = 9.7$ μm where the silicate cross section peaks (Draine 2003). This feature can produce either emission or absorption in the spectrum depending on the optical depth of the medium at this wavelength (Bjorkman & Wood 2001). In order to have absorption at this wavelength, the medium has to be optically thick (i.e., $\tau_{9.7\mu{\rm m}} \gg 1$). Generically, this would also result in deep absorption in the optical/NIR bands ($\sim$0.01–1 μm) owing to their much higher dust opacity, which is almost 2 orders of magnitude higher than that at 9.7 μm according to the dust opacity curve in Figure 4. Our spectra exhibit absorption when the system is in the starburst phase (e.g., $z \gtrsim 10$) when the object is highly obscured. As the system proceeds to the quasar phase (e.g., $z < 8$), the emission feature becomes increasingly prominent as dust becomes more and more transparent to the radiation.

In observations, both absorption and emission features at $\lambda_{\rm rest} = 9.7$ μm have been detected for a wide range of objects up to $z \sim 3$ (Armus et al. 2004; Papovich et al. 2006). An absorption feature is frequently seen in dusty star-forming galaxies such as M82 (e.g., Sturm et al. 2000), Arp 220 (e.g., Spoon et al. 2004), and ULIRG IRAS 08572+3915, which exhibits the most extreme absorption (Spoon et al. 2006). A comprehensive collection of the SEDs of starburst nuclei and ULIRGs is reviewed by Siebenmorgen & Krügel (2007), who also provide a library of 7000 SEDs for dusty galaxies.

On the other hand, an emission feature is also reported in many observations (Hao et al. 2005; Siebenmorgen et al. 2005; Sturm et al. 2005). In particular, Hao et al. (2007) analyze a sample of 196 local AGNs and ULIRGs observed by the Infrared Spectrograph (IRS; Houck et al. 2004) on board the *Spitzer Space Telescope* (Werner et al. 2004) to study the distribution of strengths of the 9.7 μm silicate feature. These authors find a wide range of silicate strengths: quasars are characterized by silicate emission and Seyfert 1 galaxies equally by emission or weak absorption. Seyfert 2 galaxies are dominated by weak silicate absorption, and ULIRGs are characterized by strong silicate absorption (mean apparent optical depth of about 1.5). Spoon et al. (2007) find that the same sample of galaxies is systematically distributed along two distinct branches: one with AGN-dominated spectra and one with deeply obscured nuclei and starburst-dominated spectra. These authors suggest that the separation may reflect a fundamental difference between the dust geometries in the sources: clumpy for AGNs versus nonclumpy obscuration for starbursts. For example, Levenson et al. (2007) suggest that the extremely deep absorption in IRAS 08572+3915 requires a source to be embedded in a smooth distribution of material that is both geometrically and optically thick. Our simulations show that the dust distribution around the quasar is quite clumpy, and that the SEDs changes from starburst to AGN-dominated as the system evolves from the starburst to quasar phases (see Fig. 16). These are consistent with the observations.

4. PARAMETER STUDIES

In this section we explore the large parameter space involved in this radiative transfer calculation, and systematically study the resolution convergence, parameters in the two-ISM model, input spectra for the black holes, the dust models, and the dust-to-gas ratios for both the cold- and hot-phase gas.

4.1. *Resolution Studies*

Figure 7 shows resolution studies for photon number (*top panel*) and grid size (*bottom panel*). The SEDs converge when the photon number is larger than 10^6. If the photon number is low, then Poisson noise is significant, which results in large fluctuations in the SEDs. Therefore, throughout the paper, we use a

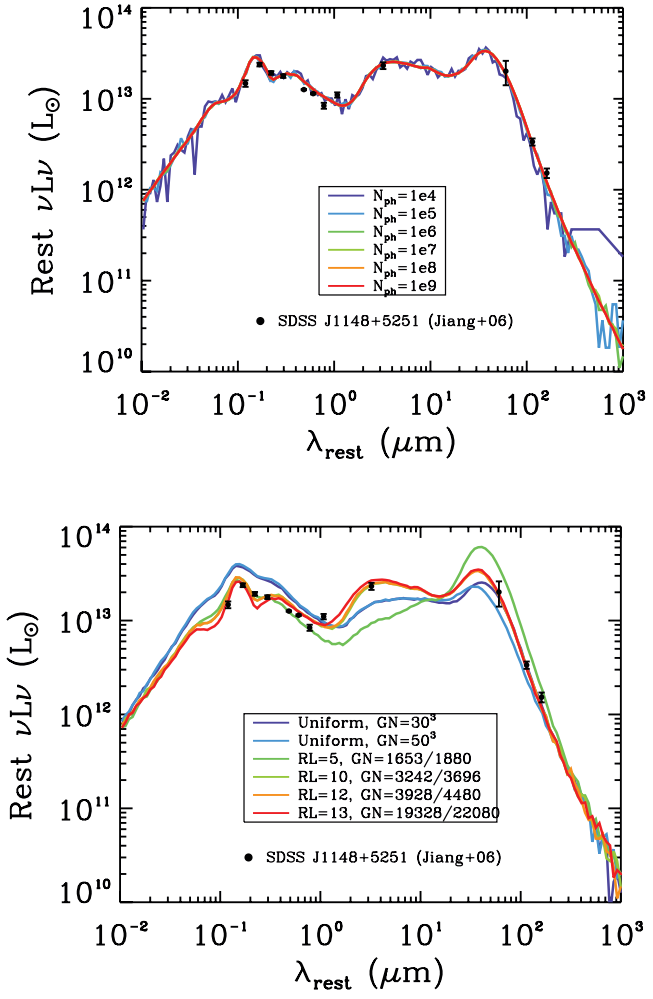

FIG. 7.—Resolution studies of the number of photons (*top*), and the grid refinement level (*bottom*), respectively. The top panel shows the SEDs produced with photon number $N_{ph} = 10^4$–10^9. These SEDs have similar shapes, and they converge when $N_{ph} \gtrsim 10^6$. A smaller photon number results in larger fluctuations in the SED owing to greater Poisson error. The bottom panel compares the SEDs produced with a uniform grid and those with adaptive grids of different refinement level. Compared to an adaptive grid method, SEDs using uniform grids with grid number GN = 30^3 and 50^3 do not have sufficient dynamic range to resolve both the cold and hot dust, which result in an underestimate of the dust emission longward of 10 μm. As the grid refinement level increases, hot dust is better resolved, contributing to the hot dust bump at 1–10 μm. The SEDs converge when the refinement level goes above 10, which has a minimum cell size approaching that of the spatial resolution of the original hydrodynamic simulations. Level 12 is the standard refinement level used in this paper.

photon number of 10^7 for SED production, and 10^8 for images in order to have a higher signal-to-noise ratio.

For the adaptive grids, as the refinement level increases, the hot dust in the central region around the AGN is better resolved, contributing to the hot dust bump in 1–10 μm. The SEDs converge when the refinement level goes above 10, which has a minimum cell size close to the spatial resolution (~30 pc) of the original hydrodynamic simulations. Compared to the adaptive grid method, SEDs using uniform grids with reasonable computing expense have poor resolution. As demonstrated in Figure 3, a 50^3 uniform grid has a resolution of 4 kpc, which can only resolve the dust in the diffuse gas in the outskirts of the system, but not the clumpy, dense regions around the central AGN. Consequently, the resulting SEDs do not entirely resolve dust emission in 1–10 μm which comes partly from hot dust near the

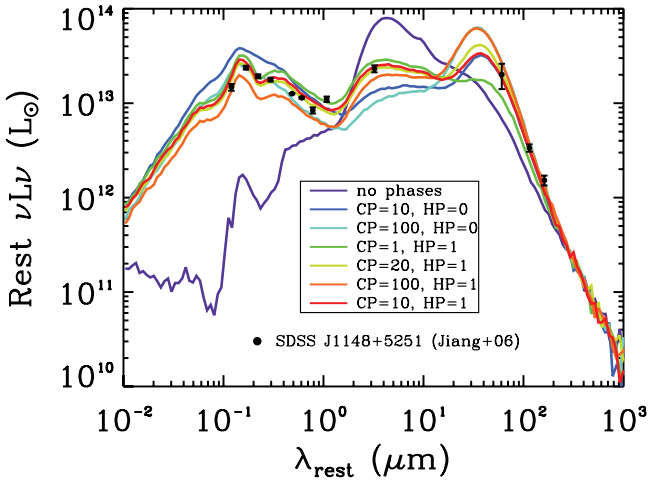

FIG. 8.—Parameter study of the two-phase break down of the ISM with hot and cold phases. In the legend, HP = 1 indicates existence of hot-phase gas, while CP = 10 indicates that the cold pressure is enhanced by a factor of 10 (see § 2.2.3 for more details). The purple curve represents the "no phase break-down" case in which the cold gas is not considered; there is only hot-phase gas whose density is the same as that given directly by the SPH simulations. The blue and cyan curves represent cases in which no hot-phase gas is present (only cold-phase gas is considered), but the pressure enhancement factor for cold-phase gas varies from 10 to 100, respectively. The rest of the colored curves represent cases in which both hot and cold phases coexist, with cold gas pressure varying from 1 to 100. In the RT calculations, we use standard values CP = 10 and HP = 1.

AGN, and the cold dust bumps are lower by up to 1 order of magnitude.

4.2. *ISM Model Parameters*

Figure 8 shows the SEDs with various parameters for the two-phase breakdown of the ISM. When there is no phase breakdown (purple curve), only hot-phase gas is considered (no cold gas). In this case, the hot gas has both large volume filling factor and mass fraction, so the extinction is extremely high, which leads to significant emission in the NIR but little emission in the 20–1000 μm range (the cold dust is sparse). In cases with cold gas only (no hot-phase gas), the SEDs show big cold dust bumps but no hot dust emission, as indicated by the blue and cyan curves. A comparison of these two curves shows that a larger cold phase pressure leads to a higher volume filling factor for the cold dust, resulting in stronger cold dust emission.

In the cases where both hot and cold phases coexist, the amount of cold dust emission depends on the cold gas pressure, as indicated by the other colored curves. We find that cold pressure in the range of 10–100 is able to produce cold dust bumps that fit the submillimeter observations of J1148+5251. However, because the SED with CP = 10 has both the hot and cold dust bumps that agree better with the mean SEDs of luminous quasars in the Sloan samples of Richards et al. (2006), we choose CP = 10 as a standard value in our calculations.

Figure 9 shows a study of the output SEDs obtained by varying the power-law indices of both the mass spectrum and the mass-radius relation of the cold clouds. Increasing α would steepen the cloud mass function, leading to more smaller cold clouds that boost the cold dust bump. A similar effect is seen by increasing β. However, the SEDs are not very sensitive to the change of either α or β in the ranges of 1.5–2.5 and 1.5–3.0, respectively. Changing α from 1.5 to 2.5, or β from 1.5 to 3.0, only results in a change in the SED by a factor of about 2. In the RT calculations, we adopt the standard values of $\alpha = 1.8$ and $\beta = 2.0$, as

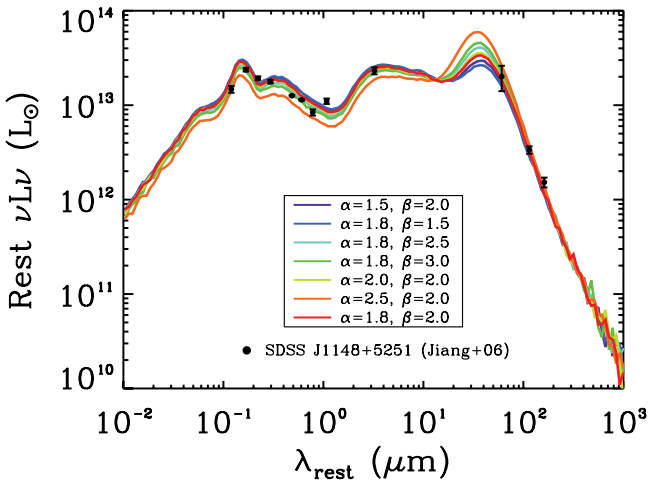

FIG. 9.—Parameter study of the power-law indices of the mass spectrum α and mass-radius relation β of the cold clouds (see § 2.2.3 for more details). The output SED is not sensitive to the ranges of α and β considered here. In the RT simulations, we adopt $\alpha = 1.8$ and $\beta = 2.0$ as suggested by observations.

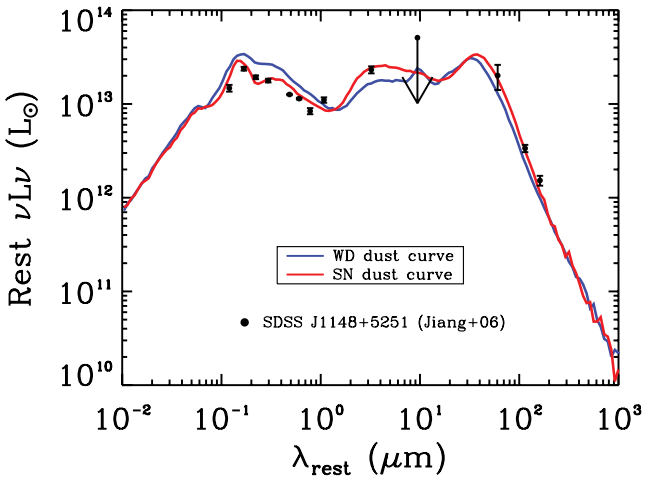

FIG. 11.—Comparison of the SEDs from using the dust extinction curves of Weingartner & Draine (2001) with $R_V = 3.1$ (WD model) and that from Type II supernovae (SN model). The arrow at ~9.43 μm indicates a 2 σ upper limit. J1148+5251 was observed with MIPS at 70 μm but with no detection. The arrow indicates a 2 σ upper limit. The current observations cannot distinguish between these two dust models.

suggested by observations (Blitz & Rosolowsky 2006; Rosolowsky 2007).

4.3. *Input Spectrum*

Figure 10 shows a comparison of the emergent SEDs using different input black hole spectrum, namely, a broken power law as in Marconi et al. (2004; *blue curve*), and a composite spectrum from Hopkins et al. (2007d; *red curve*). All other parameters being equal, the SED using the power-law spectrum shows more emission in the optical bands and lower emission in the IR than the SED with the composite input spectrum. These differences owe their origin to differences in the input spectrum. The composite spectrum includes emission from hot dust residing in the vicinity of the AGN that is below the resolution limit of our hydrodynamic simulations. This figure emphasizes the care that must be taken when including an AGN and performing radiative transfer on scales that are not well resolved, and demonstrates that a composite black hole spectrum as in Hopkins et al. (2007d) provides a viable subresolution prescription for the dust emission contributed within parsecs of the AGN.

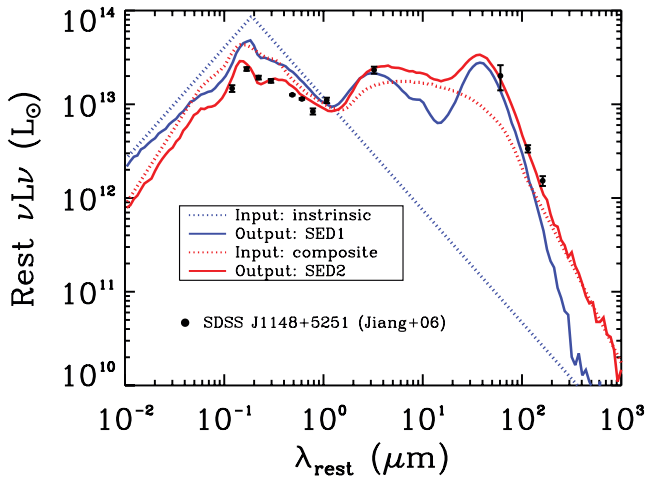

FIG. 10.—Parameter study of the input spectrum for the black hole. The solid curves represent the output SEDs, while the dotted lines represent the input black hole spectra. The blue and red curves indicate the use of an intrinsic, broken power law as in Marconi et al. (2004) and a composite spectrum from Hopkins et al. (2007d), respectively. Both input spectra have the same bolometric luminosity. A power-law input spectrum would require parsec-scale resolution to resolve the dust near the AGN in order to produce the NIR emission, which is below the resolution of our hydrodynamic simulations. A composite spectrum therefore serves as a subresolution recipe to resolve the dust emission within parsecs of the AGN.

4.4. *Dust Models*

Figure 11 shows the emergent SEDs using dust extinction curves from the WD model (Weingartner & Draine 2001) with $R_V = 3.1$ and our SN model, respectively. The SEDs agree well at wavelengths $\lambda \gtrsim 10$ μm, but differ by a factor of a couple in the optical/NIR bands 0.1–10 μm. It appears that WD model would require a higher dust-to-gas ratio than that of the Milky Way by a factor of a few in order to produce the observed SED of J1148+5251. In such case, the WD model would produce a stronger peak at the 9.7 μm silicate feature by a similar factor relative to the SN model. Observation of J1148+5251 at ~9.7 μm would be helpful in distinguishing between these two models. However, the current data point at that wavelength (observed by MIPS at 70 μm) is only a 2 σ upper limit, insufficient to constrain the model.

As discussed in § 2.2.4, Elvis et al. (2002) suggest that quasars may also be copious producers of dust, as condensation in quasar outflows is similar to dust formation in the envelopes of AGB stars. In this case, the dust extinction curve would be similar to the WD model. However, the contribution of dust from quasar winds in the early universe remains unknown. The recent report by Stratta et al. (2007) of dust extinction in the host galaxy of GRB 050904 at $z = 6.3$ independently supports a supernova-origin dust model. If both supernovae from starbursts and quasar outflows play important roles in dust production in these young quasar systems at $z \sim 6$, then the resulting dust extinction curve would be intermediate to the WD and SN models shown in Figure 11. More observations and deeper surveys for dust in high-z galaxies and quasars will be necessary to constrain dust formation mechanisms at early cosmic times.

4.5. *Dust-to-Gas Ratios*

It has been suggested that ULIRGs have dust-to-gas ratio (mostly cold gas as in our modeling) close to that of the Milky

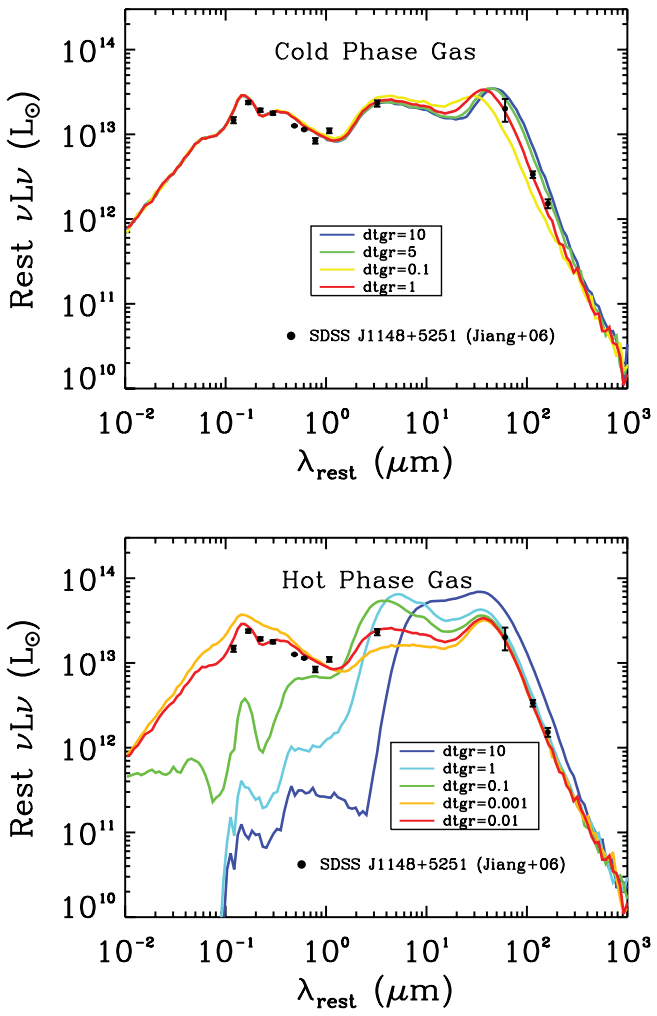

FIG. 12.—Parameter study of the dust-to-gas ratio relative to Milky Way value, for the cold-phase gas (CPG; *top panel*) and hot-phase gas (HPG; *bottom panel*), respectively. This figure shows that the emergent SED is more sensitive to the dust-to-gas ratio of the HPG than to the CPG owing to the large covering factor of the HPG. In the regular RT calculations, the default values are 1 and 1% of the Milky Way value for CPG and HPG, respectively.

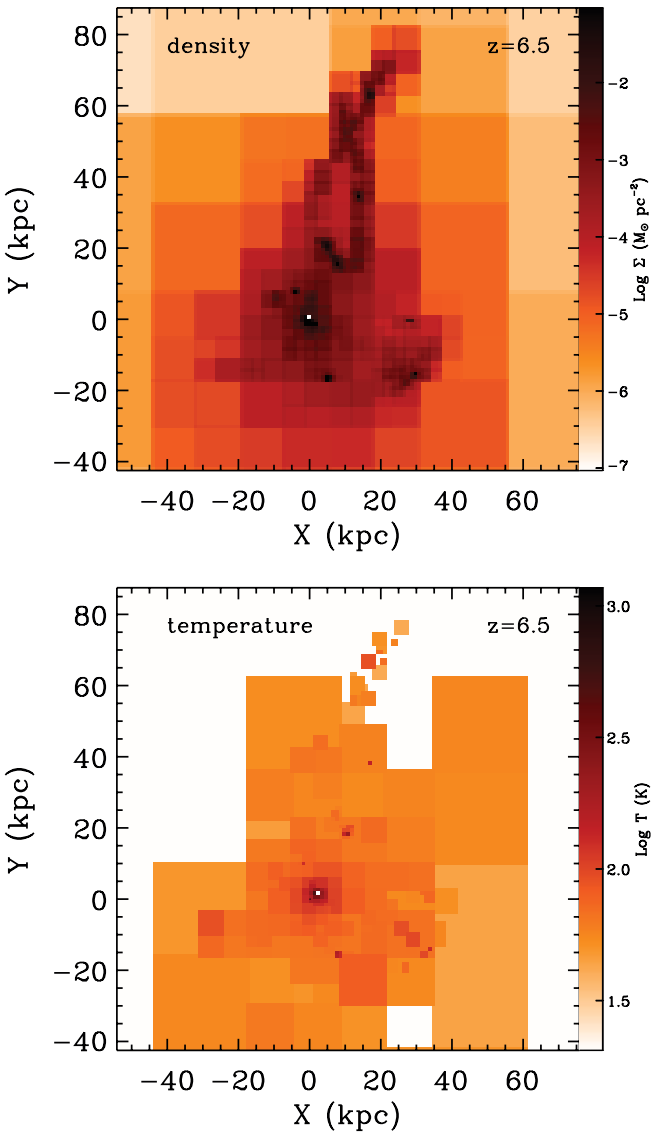

FIG. 13.—Maps of the projected density (*top*) and temperature (*bottom*) of the HPG dust (dust associated with hot phase gas). The origin of the map is the location of the central quasar, and the coordinates are comoving. Note that the gas only determines the distribution and mass of the dust; the dust temperature is not associated with the gas temperature but is calculated self-consistently from the radiation field (see § 2.2.3 for more details).

Way (e.g., Dunne & Eales 2001; Klaas et al. 2001). While some observations of obscured, X-ray-selected AGNs seem to suggest that the dust-to-gas ratio in these objects has a wide range, from $\sim 10^{-3}$ to a few of MW (Milky Way) value (e.g., Maiolino et al. 2001; Kuraszkiewicz et al. 2003; Hall et al. 2006). Although this range may apply mainly to the hot, fully or partially ionized gas in the circumnuclear regions of the AGNs, it would be interesting to see how such a range affects the output SED in our calculations.

Figure 12 shows the comparison of the emergent SEDs with different dust-to-gas ratios in a wide range, for both cold (*top panel*) and hot-phase gases (*bottom panel*), respectively. The values in the plot are relative to the MW value. A change of 2 orders of magnitude in the dust-to-gas ratio of the cold phase gas results in a difference in the cold dust bump only by a factor of a few. However, a similar change in the dust-to-gas ratio in the hot phase gas would result in substantial difference in the output SED. This study shows the extinction is dominated by the hot dust, which has a much larger covering factor that the cold dust. We find that using 1 and 1% of MW value for the cold and hot phase gas, respectively, reproduce the observation of SDSS J1148 reasonably well. Therefore, we elect to use them as default values for our standard RT calculations. Note this choice of 1% of MW value for the hot, diffuse gas has little effect for the starburst or ULIRG phase, because a substantial fraction of gas during that stage is in the cold clouds. However, it may affect the SEDs of major quasar phase, as the gas is heated by the AGN. We should point out that in our ISM model, we do not have the warm phase as in the picture of McKee & Ostriker (1977). Such a warm phase medium may have a dust-to-gas ratio similar to that of MW. We will explore such a treatment in future work.

5. THE DUST DISTRIBUTION

The distribution of dust is essential to investigating dust formation mechanisms and heating sources. Figure 13 shows the projected spatial distribution of the dust density and temperature in the system at $z = 6.5$. The projected quantity is calculated with $\int f(l)\, dl/L$, where $f(l)$ is density or temperature distribution along the line of sight, while L is the total length of the sight line. Gravitational torques in the interaction produce strong shocks and

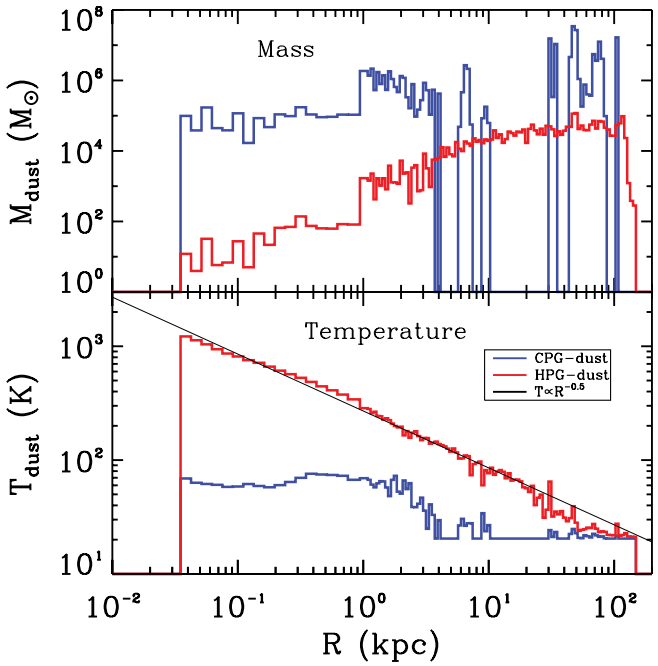

FIG. 14.—Radial distribution of dust mass (*top*) and temperature (*bottom*) as a function of the distance from the central AGN. The blue and red curves represent the CPG and HPG dust, respectively, while the black curve in the bottom panel is a power-law temperature profile, $T \propto R^{-1/2}$ as expected from heating by the central AGN.

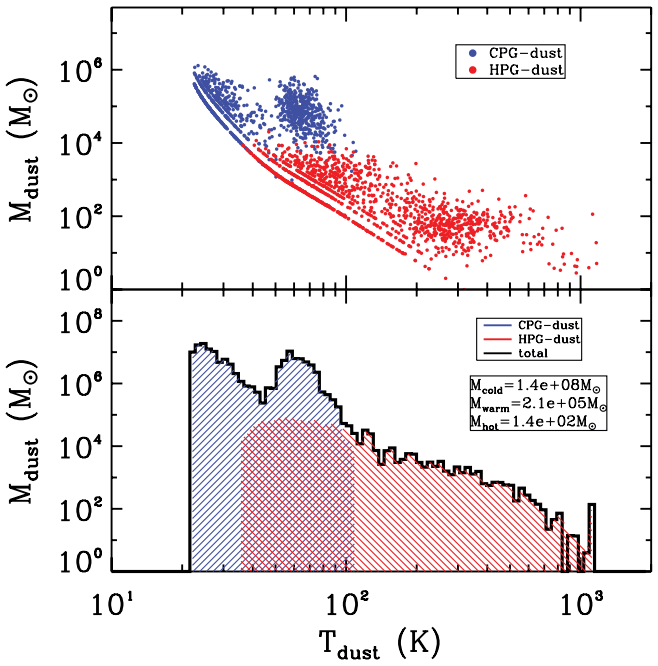

FIG. 15.—Mass-temperature distribution of both the CPG (*blue*) and HPG dust (*red*). In the bottom panel, M_{cold}, M_{warm}, and M_{hot} represent the total mass of cold, warm, and hot dust with $T \lesssim 100$ K, $100 < T < 1000$ K, and $1000 \lesssim T \lesssim 1200$ K, respectively.

tidal features, making the dust distribution highly inhomogeneous and clumpy. The dynamic range in density can be up to 6 orders of magnitude. Both the dust density and temperature peak in the central regions near the AGN.

The detailed radial distributions of the dust mass and temperature are quantified in Figure 14. The blue and red curves in this figure represent CPG and HPG dust, dust associated with cold- and hot-phase gas, respectively, as defined in § 2.2.3. The CPG dust has high density but a small volume filling factor; it is generally optically thick to radiation. On the other hand, the HPG dust has a lower density but fills $\gtrsim$99% of the volume, and is generally optically thin. Both the dust mass and temperature vary with distance from the central AGN. The cold dust is typically surrounded by hot dust. In the inner hundred parsecs, the cold cores are highly condensed and are optically thick even to the hard radiation from the black hole. However, the HPG dust at the edges surrounding these cold cores is heated directly by the central AGN. This is indicated by the power-law temperature profile in the lower panel of Figure 14, $T \propto R^{-1/2}$ as expected from equation (4): $T^4(R) \propto E(R) \propto R^{-2}$. The hottest dust is heated up to $\sim$1200 K, which is below the dust sublimation temperature $\sim$1600 K (Hönig et al. 2006). Cooler dust ($T \sim$ tens to hundreds K) is distributed in an extended region from $\sim$100 pc to several kiloparsecs. The heating sources come both from stars and the central AGN. Beyond 10 kpc, the dust temperature drops to below 100 K. Note that the minimum temperature in Figure 14 is $\sim$20 K, which is the CMB temperature at $z = 6.5$.

Figure 15 shows histograms of the dust mass and temperature. The dust temperature ranges from $\sim$10–10^3 K. The amount of the hottest dust ($\sim 10^3$ K) is $\sim 1.4 \times 10^2\ M_\odot$, while that of the cold dust ($T \lesssim 10^2$ K) is $\sim 1.4 \times 10^8\ M_\odot$. This is in agreement with the estimates of the dust detected in the host of J1148+5251 (Bertoldi et al. 2003a; Beelen et al. 2006; Jiang et al. 2006).

The large amount of cold dust ($\sim 1.4 \times 10^8\ M_\odot$) located within 3 kpc from the AGN provides efficient cooling for the formation of molecular gas. In Narayanan et al. (2007) we calculate carbon monoxide emission using a nonlocal thermodynamic equilibrium radiative transfer code (Narayanan et al. 2006a, 2006b), and find that CO gas forms in this region, with a total mass of $\sim 10^{10}\ M_\odot$, similar to observations by Walter et al. (2004). This suggests that cold dust and molecular gas are closely associated, and both depend on the star formation history. Our results show that significant metal enrichment takes place early in the quasar host, as a result of strong star formation in the progenitors, and that intense starbursts (SFR $\gtrsim 10^3\ M_\odot\ \mathrm{yr}^{-1}$) within $\lesssim 10^8$ yr are necessary to produce the observed properties of dust and molecular gas in the host of J1148+5251, a conclusion which is also supported by the analytical models of Dwek et al. (2007).

6. EVOLUTION OF THE QUASAR SYSTEM

6.1. *Transition from Cold to Warm ULIRG*

In Li et al. (2007) we show that the host of the $z \sim 6$ quasar undergoes hierarchical mergers starting from $z \sim 14$, and the quasar descends from starburst galaxies. The evolution of the SEDs of the system in the observed frame is shown in Figure 16. Note that absorption of the Lyman lines and continuum by the intergalactic medium (Madau 1995) is taken into account. During early stages at $z \sim 14$, the SED of the quasar progenitor shows only a cold dust bump that peaks around $\sim$60 μm, which is characteristic of starburst galaxies (Sanders & Mirabel 1996). As the system evolves from starburst to quasar phases, dust extinction in the UV-optical bands increases, boosting the emission reprocessed by dust at wavelengths longward of 1 μm. The gradually increasing radiation from the accreting black holes heats the nearby dust to high temperatures, contributing to the hot dust bump which peaks around $\sim$3 μm (rest frame). At the maximum quasar phase at $z \simeq 6.5$ indicated by the red curve, the hot dust bump SED reaches its peak with a temperature of $\sim$1200 K, as we have seen in the previous section. Such an SED represents luminous, blue quasars in the samples of Jiang et al. (2006) and

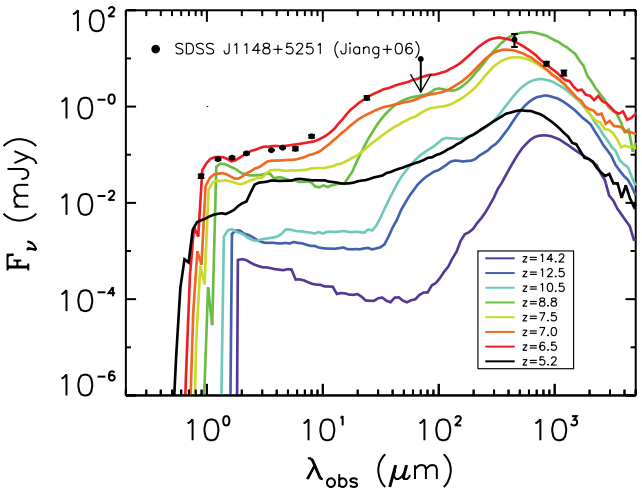

FIG. 16.—Evolution of the SEDs of the quasar system and its galaxy progenitors in the observed frame. The colored curves represent SEDs from $z \sim 14$ to $z \sim 5.2$, while the black dots are again observations from Jiang et al. (2006), as described in the legend. Absorption of the Lyman line series and continuum by the intergalactic medium (Madau 1995) is taken into account, which results in a sharp drop at short wavelengths.

Richards et al. (2006). As the system ages and reddens in the postquasar phase (*black curve*), the total luminosity of the system drops. However, there is still some residual hot dust, and the infrared luminosity is dominated by the NIR and IR. This resembles the class of infrared-bright, optically red quasars found in recent surveys (e.g., Brand et al. 2006). Overall, the evolution of the SED from a starburst to a quasar can be characterized by the slope of the infrared SED (3–50 μm), as it decreases from the starburst to quasar phases owing to the increase of NIR emission from the hot dust heated by the AGN.

Infrared luminosities are powerful tools to study starburst galaxies and quasars. From the results in the previous sections, we see that the emission in NIR (1–10 μm), mid-IR (10–40 μm), and FIR (40–120 μm) comes from reemission by hot, warm, and cold dust, respectively. Note that the meaning of FIR varies in the literature. Here we use the definition of FIR given by Condon (1992) in order to compare our results with the observations by Carilli et al. (2004), who used the same FIR range.

Using $L_{\rm IR}$ (8–1000 μm), Sanders & Mirabel (1996) classified infrared luminous galaxies into three categories, namely, luminous infrared galaxies (LIRGs; $L_{\rm IR} > 10^{11}\ L_\odot$), ultra-LIRGs (ULIRGs; $L_{\rm IR} > 10^{12}\ L_\odot$), and hyper-LIRGs (HLIRGs, $L_{\rm IR} > 10^{13}\ L_\odot$). Figure 17 (*top*) shows the evolution of the infrared luminosities of the quasar system in our simulations. The luminosities increase with the star formation rate and black hole accretion rate. The system is ultraluminous most of the time, with periods in HLIRG phases associated with bursts of star formation or quasar activity. When the last major mergers take place between $z \sim 9$–7.5, the strong shocks and highly concentrated gas fuel rapid star formation and black hole growth. This also produces a large amount of dust heated by the central AGN and stars. As a result, the infrared luminosities increase dramatically, pushing the system to HLIRG class.

The infrared luminosities strongly peak at $z \sim 8.7$ when the star formation rate reaches $\gtrsim 10^4\ M_\odot\ {\rm yr}^{-1}$, suggesting a significant contribution from stars in heating the dust to emit in the range 1–1000 μm. During the major quasar phase ($z \sim 7.5$–6) the star formation declines to $\sim 10^2\ M_\odot\ {\rm yr}^{-1}$, and the emission in NIR and MIR outshines that in FIR, demonstrating that AGNs can play a dominant role in heating the dust and producing NIR and MIR

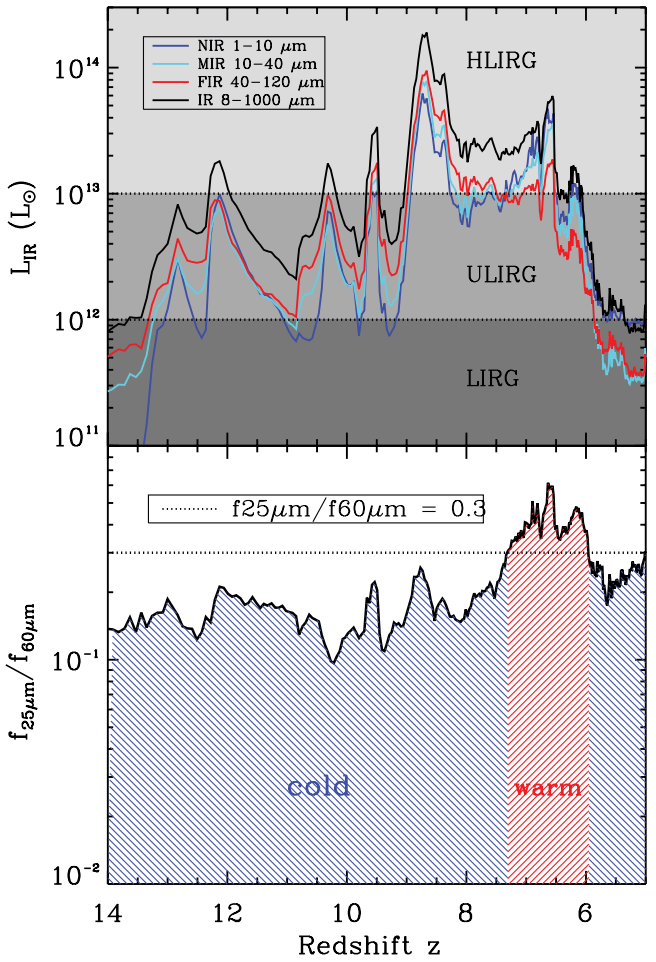

FIG. 17.—Evolution of rest-frame infrared luminosities of the quasar system (*top*) and the rest-frame color $f_{25\ \mu{\rm m}}/f_{60\ \mu{\rm m}}$ (*bottom*). In the top panel, the solid curves represent the luminosity in near-IR (1–10 μm), mid-IR (10–40 μm), far-IR (40–120 μm), and IR (8–1000 μm), respectively. The gray shades indicate regimes for LIRG ($L_{\rm IR} > 10^{11} L_\odot$), ULIRG ($L_{\rm IR} > 10^{12}\ L_\odot$), and HLIRG ($L_{\rm IR} > 10^{13}\ L_\odot$), respectively, as classified by Sanders & Mirabel (1996). The ratio $f_{25\ \mu{\rm m}}/f_{60\ \mu{\rm m}}$ in the bottom panel is an indicator of the coldness of the SED with a critical value of 0.3 (Sanders & Mirabel 1996). The quasar system in our model evolves from "cold" ULIRG ($f_{25\ \mu{\rm m}}/f_{60\ \mu{\rm m}} < 0.3$) to "warm" ULIRG (including HLIRG, $f_{25\ \mu{\rm m}}/f_{60\ \mu{\rm m}} \geq 0.3$) as it transforms from starburst to quasar phases.

emission. Furthermore, the AGN can also contribute to FIR emission. For example, while the star formation rate drops by a factor of $\sim$500 from $z \sim 8.7$ (when star formation rate peaks) to $z \sim 6.5$ (when black hole accretion rate peaks; see Fig. 1), the $L_{\rm FIR}$ declines by only a factor of $\sim$50, indicating substantial contribution to the $L_{\rm FIR}$ by the AGN. This significant AGN contribution has important implications for estimating the star formation rate. We will discuss this issue at length in the next section. During the "postquasar" phase at $z < 6$, as a result of feedback which suppresses both star formation and black hole accretion, and gas depletion which reduces the amount of dust, the infrared luminosities drop rapidly.

The flux ratio $f_{25\ \mu{\rm m}}/f_{60\ \mu{\rm m}}$ is a color indicator for the coldness of the SED, and can be used as a diagnostic for AGN activity, as suggested by Sanders & Mirabel (1996). For example, starburst galaxies usually have cold colors $f_{25\ \mu{\rm m}}/f_{60\ \mu{\rm m}} < 0.3$, while quasars are warm with $f_{25\ \mu{\rm m}}/f_{60\ \mu{\rm m}} \gtrsim 0.3$. The evolution of the color $f_{25\ \mu{\rm m}}/f_{60\ \mu{\rm m}}$ of the simulated quasar system is shown in Figure 17 (*bottom*). The color index is below 0.3 most of the time, i.e., during both starburst- and postquasar phases. However, it rises

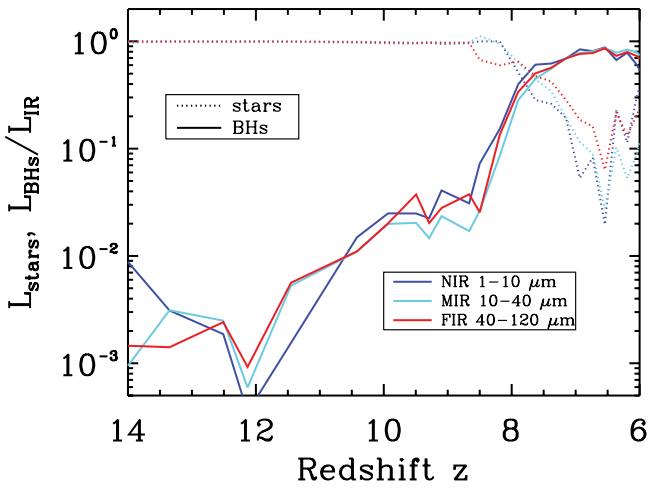

FIG. 18.—Contribution to the infrared luminosities, L_{NIR}, L_{MIR}, and L_{FIR}, from both AGNs and stars, respectively. During the starburst phase, stars are the main heating source for the infrared emission. However, during the peak quasar phase, AGN heating dominates.

above 0.3 during the short quasar phase. This figure clearly demonstrates that the system evolves from a cold to warm ULIRG (including HLIRG) as it transforms from starburst to quasar phases. Similar trend is also reported by Chakrabarti et al. (2007a). Our results provide further theoretical support for the starburst-to-quasar conjecture, as suggested by observations (Sanders & Mirabel 1996; Scoville 2003).

6.2. *AGN Contamination and the* SFR-L_{FIR} *Relation*

AGN contamination in infrared observations of dusty, star-forming quasar systems has been a long-standing problem. In our simulations, we see that the contributions from AGNs and stars both vary according to the activity of these two populations. As shown in Figure 18, during the starburst phase, not surprisingly nearly all the infrared emission comes from dust heated by stars. However, during the peak quasar phase, the contribution from the AGN dominates the infrared light production in the system. This result has significant implications for the interpretation of observational data, such as estimates of the star formation rate.

In particular, owing to the lack of other indicators such as UV flux or Hα emission, in observations of high-redshift objects the far-infrared luminosity is commonly used to estimate the star formation rate, assuming most or all of L_{FIR} is contributed by young stars. For example, J1148+5251 has $L_{FIR} \sim 2 \times 10^{13}\ L_{\odot}$, and the star formation rate is estimated to be $\sim 3 \times 10^{3}\ M_{\odot}\ \mathrm{yr}^{-1}$ (Bertoldi et al. 2003a; Carilli et al. 2004). However, these studies cannot rule out a substantial contribution (e.g., ~50%) to L_{FIR} by the AGN. If L_{FIR} is indeed heavily contaminated by AGN activity, then the SFR-L_{FIR} relation would be invalid, and the actual star formation rate would be much lower.

To demonstrate this, we show in Figure 19 the SFR-L_{FIR} relation in three cases: (1) only black holes are included as a heating source of the dust (*top*); (2) only stars are included (*middle*); and (3) both black holes and stars are included (*bottom*). The top panel shows that there is no correlation between the SFR and the L_{FIR} which is produced by AGNs. However, if all the L_{FIR} is produced solely from stars, then there is a tight, linear correlation. If the L_{FIR} is contributed by both AGN and stars, then the correlation would change. The bottom panel in Figure 19 shows that during the starburst phase where stars dominate dust heating, there is still a correlation between SFR and L_{FIR} with modified

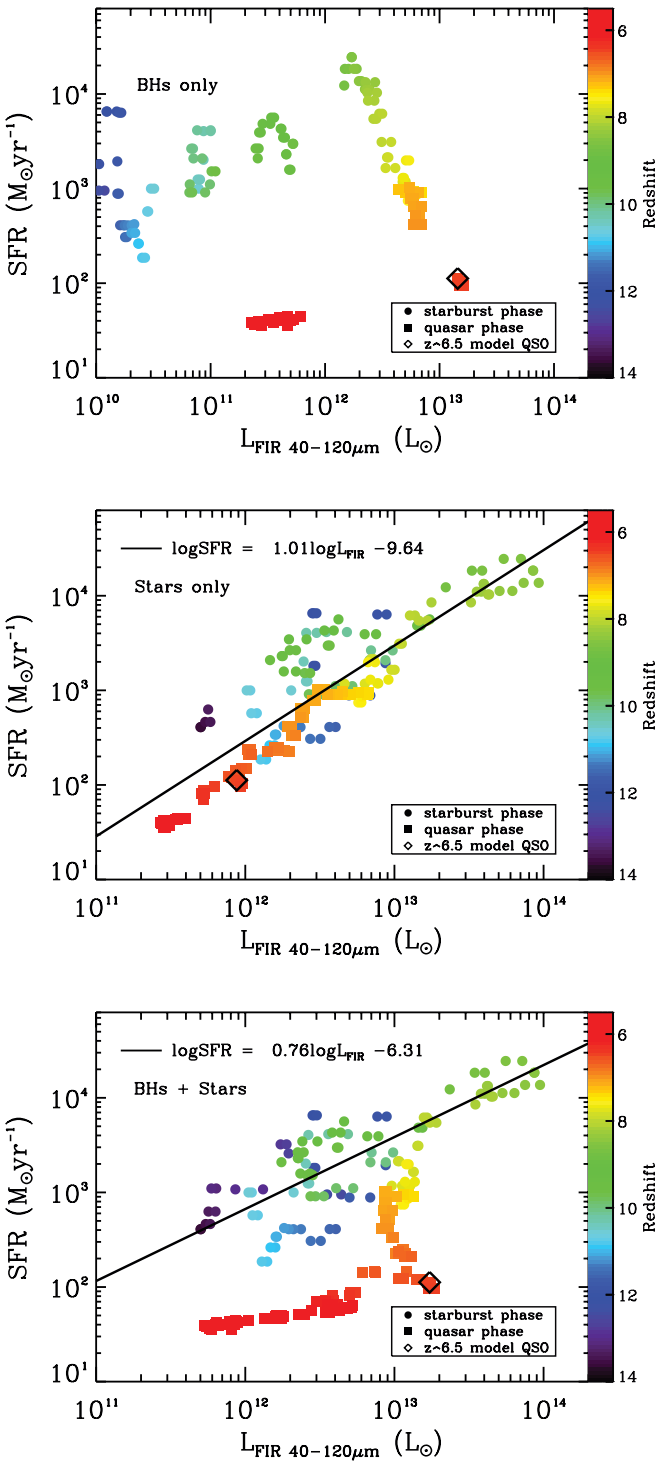

FIG. 19.—Evolution of the SFR-L_{FIR} relation in our simulations. Here we consider the relation in three cases where L_{FIR} is contributed by AGNs only (case 1; *top*), stars only (case 2; *middle*), and both AGNs and stars (case 3; *bottom*). The colored filled symbols indicate the system at different redshifts, while the black open diamond represents the model quasar at $z = 6.5$. The black curve in the middle panel is the least-squares fit to all the data, while that in the bottom panel is the fit to data points from $z \sim 14$–7.5 only (starburst phase). Case 1 has no SFR-L_{FIR} correlation; case 2 has a tight, linear correlation similar to that used in observations; and case 3 has a nonlinear correlation.

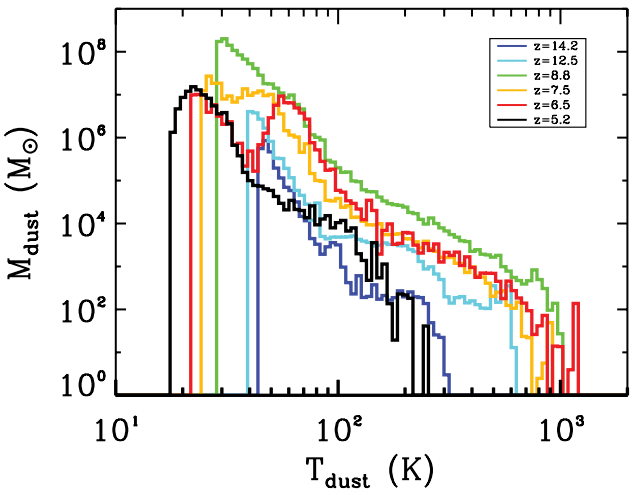

FIG. 20.— Evolution of the dust mass and temperature as a function of redshift. The dust is heated by both stars and AGNs. As the system evolves from starburst to quasar phases, the amount of hot dust increases. The dust reaches the highest temperature during the peak quasar phase. After that, the dust cools owing to the decline of AGN radiation.

slope and normalization. However, during the peak quasar phase where the AGN dominates dust heating, there is no correlation at all. To summarize, Figure 19 gives the following SFR-$L_{\rm FIR}$ relations:

$$\frac{\rm SFR}{M_\odot\ {\rm yr}^{-1}} = 2.3\times10^{-10}\left(\frac{L_{\rm FIR}}{L_\odot}\right)^{1.01}\ \text{(stars only)}, \qquad (21)$$

$$\frac{\rm SFR}{M_\odot\ {\rm yr}^{-1}} = 4.9\times10^{-7}\left(\frac{L_{\rm FIR}}{L_\odot}\right)^{0.76}\ \text{(AGNs + stars)}. \qquad (22)$$

Here, the FIR is in the range of 40–120 μm (rest frame). This correlation in the stars-only case is very close to that found by Kennicutt (1998b) (SFR/$M_\odot$ yr^{-1}) $\simeq 1.7\times10^{-10}(L_{\rm FIR}/L\odot)$ for starburst galaxies. Note the slight difference in the normalization might owe to different stellar IMFs used—we use the top-heavy Kroupa IMF (Kroupa 2002), while Kennicutt (1998b) adopts a Salpeter IMF (Salpeter 1955). Also, the $L_{\rm FIR}$ in that work refers the infrared luminosity integrated over the range of 8–1000 μm.

In our simulation, the model quasar at $z = 6.5$ has $L_{\rm FIR} \simeq 1.8\times10^{13}\ L_\odot$, which is close to that of J1148+5251 derived from radio observation (Bertoldi et al. 2003a; Carilli et al. 2004). If we assume a perfect SFR-$L_{\rm FIR}$ correlation as in the middle panel of Figure 19 (eq. [21]), then the SFR would be $\sim4\times10^3\ M_\odot$ yr^{-1}, similar to the estimate of Bertoldi et al. (2003a); Carilli et al. (2004). However, the SFR of the model quasar from our simulations is about $\sim112\ M_\odot$ yr^{-1}, which is significantly lower than that derived from an ideal SFR-$L_{\rm FIR}$ correlation. This discrepancy is largely due to significant contribution to the $L_{\rm FIR}$ by AGN activity. Several studies by Bertoldi et al. (2003a); Carilli et al. (2004) and Wang et al. (2007) find that most $z \sim 6$ quasars do not seem to show a $L_{\rm FIR}$-L_B correlation, but instead follow a strong $L_{\rm FIR}$-$L_{\rm radio}$ correlation as measured in local star-forming galaxies (Condon 1992). These authors therefore suggest that these $z \sim 6$ quasars are strong starbursts, and that most of the $L_{\rm FIR}$ may come from stars. However, the $L_{\rm FIR}$-$L_{\rm radio}$ correlation may not guarantee the stellar origin of the $L_{\rm FIR}$ as the physical basis for this correlation is unknown. Our results suggest that in quasar systems, $L_{\rm FIR}$ alone may no longer be a reliable estimator for star formation rates; other diagnostics should also be considered. We will study this topic with more detail in a future paper by investigating the correlations in a multiple luminosity plane, L_B-$L_{\rm FIR}$-$L_{\rm X\text{-}ray}$-$L_{\rm radio}$, of starburst galaxies and quasars.

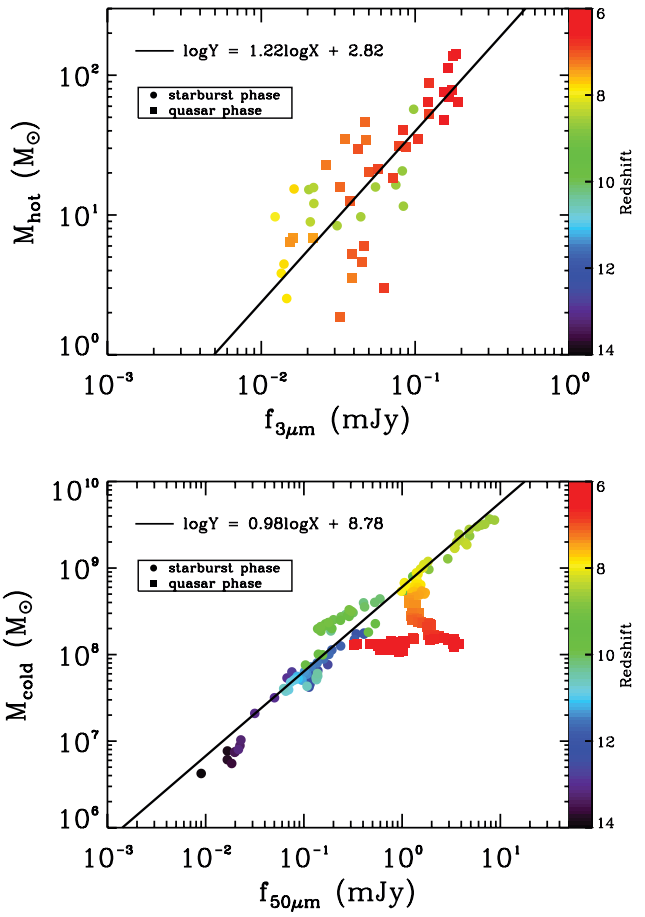

FIG. 21.— Relations between rest-frame flux $f_{3\,\mu\rm m}$ and hot dust mass $M_{\rm hot}$ (*top*), and $f_{50\,\mu\rm m}$ and cold dust mass $M_{\rm cold}$ (*bottom*). The black curve is the least-squares fit to all the data in top panel, and data during starburst phase at redshift $z \sim 14$–7.5 in bottom panel.

6.3. *Evolution of the Dust Properties*

Figure 20 shows the evolution of the dust properties, including the dust mass and temperature, as a function of redshift. As the system evolves from starburst to quasar phases, the amount of hot dust increases accordingly owing to the enhanced heating from the central AGN, as well as replenishment of gas/dust from incoming new galaxy progenitors during mergers. The amount of cold dust ($T \lesssim 100$ K) reaches a maximum at $z \sim 8.8$ when the last major merger takes place, then decreases steadily as the dust is heated to higher temperatures, or as the gas is consumed by star formation and black hole accretion. Strong star formation is able to heat the dust nearly to $T \sim 1000$ K. However, the hottest dust at $T \sim 1200$ K is associated only with the peak quasar phase at $z \sim 6.5$ when the hot dust is directly heated by the AGN. After that, the amount of hot dust drops dramatically as a result of the rapidly declining radiation from the central AGN.

In observations, the dust mass is usually determined by assuming that the dust radiates as a black- or graybody (Hughes et al. 1997; Jiang et al. 2006). In the emergent SEDs from our radiative transfer calculations, the cold dust bumps at different

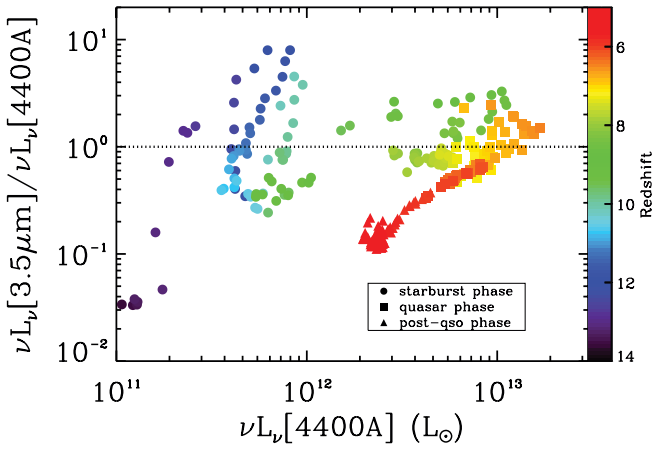

FIG. 22.— Evolution of the relation between rest-frame 3.5 μm luminosity and B-band luminosity (4400 Å) for the quasar system in our simulations. The filled circles represent starburst phases, squares represents quasar phases, and triangles represent postquasar phases. Colors indicates redshift of the object.

redshifts appear to peak around ~50 μm (rest frame), while the hot dust bumps peak around ~3 μm. Figure 21 shows the relations between the dust mass and fluxes at these two wavelengths. The top panel shows that $M_{\rm hot}$ ($T \gtrsim 10^3$ K) increases with $f_{3\,\mu{\rm m}}$ flux, while $M_{\rm cold}$ ($T \lesssim 10^2$ K) correlates with $f_{50\,\mu{\rm m}}$ flux linearly during the starburst phase:

$$\frac{M_{\rm hot}}{M_\odot} = 4.2\times10^2 \left(\frac{f_{3\,\mu{\rm m}}}{\rm mJy}\right)^{1.22}, \quad (23)$$

$$\frac{M_{\rm cold}}{M_\odot} = 6.0\times10^8 \left(\frac{f_{50\,\mu{\rm m}}}{\rm mJy}\right)^{0.98}. \quad (24)$$

However, during the quasar phase, there appears to be an excess in $f_{50\,\mu{\rm m}}$, so the $M_{\rm cold}$-$f_{50\,\mu{\rm m}}$ correlation does not apply. These results suggest that rest-frame 3 and 50 μm might serve as good diagnostics for dust, the former for hot dust in quasar systems, and the latter for cold dust in starburst galaxies.

It has been suggested by Jiang et al. (2006) that the NIR-to-optical flux ratio may be used to probe dust properties. From a sample of 13 $z \sim 6$ quasars observed with *Spitzer*, these authors find that two quasars have a remarkably low flux ratio (rest-frame 3.5 μm to B-band) compared to other quasars at different redshifts, and they are also weak in FIR. Furthermore, such a low flux ratio was not seen in low-redshift quasar counterparts. These findings lead to the suggestion that these two quasars may have different dust properties from others (Jiang et al. 2006).

From our model, we find that the dust properties are associated with the evolutionary stages of the host. Figure 22 shows the evolution of the ratio $L_{\rm NIR}/L_B$ from the quasar system at different stages of its life. Early on, during the starburst phase, the ratio $L_{\rm NIR}/L_B$ is low. As the system proceeds to its peak quasar activity, the heating from the central AGN increases the hot dust emission around 3 μm, boosting the $L_{\rm NIR}/L_B$ ratio. After that, in the post-quasar phase, as the radiation from the AGN declines, the hot dust emission drops rapidly, resulting in a lower $L_{\rm NIR}/L_B$. According to our model, there might be two possible explanations for the two outliers in the Jiang et al. (2006) sample. One possibility is that they may be young quasars that are still in the starburst phase but have not yet reached peak quasar activity, so the light from star formation may be dominant or comparable to that from the accreting SMBH still buried in dense gas. This may explain the low NIR flux, as well as the B-band luminosity and the narrow Lyα emission line, which are primarily produced by the starburst. From Figure 17, we note that there are "valleys" between major starbursts (or mergers) where the infrared luminosities are low. This may explain the weak FIR in these two quasars. Another possibility is that these two objects may be in the post-quasar phase, which would also have low $L_{\rm NIR}/L_B$ and FIR (see also Figs. 17 and 19).

However, our model predicts that the same evolution should apply to every luminous quasar formed in gas-rich mergers. It cannot explain statistically why such a low $L_{\rm NIR}/L_B$ ratio is only found in the $z \sim 6$ quasars, but not at low redshifts. Perhaps these two quasars indeed have unusual dust properties that cannot be explained by our current model. More observations of dust in high-z objects are needed to resolve the issues surrounding the IR-weak quasars in Jiang et al. (2006) and to test our model.

7. DISCUSSION

Our three-dimensional Monte Carlo radiative transfer code ART^2 makes it possible to calculate self-consistently the radiative transfer and dust emission from galaxies and quasars which have large dynamic ranges and irregular geometries. It works efficiently on hydrodynamics simulations of galaxies and mergers, and has flexible grid resolution that can be adjusted to any SPH resolution in hydrodynamic simulations.

To date, only a limited number of RT calculations have been performed on galaxy mergers (Jonsson 2006; Chakrabarti et al. 2007a, 2007b). In particular, the parallel SUNRISE code developed by Jonsson (2006) marked a milestone in this direction. It has an adaptive grid similar to ours and works efficiently on the arbitrary geometry in galaxy mergers. However, radiative equilibrium is not yet included in this code, so SUNRISE cannot currently calculate dust emission self-consistently.

On the other hand, Chakrabarti et al. (2007a, 2007b) had a similar approach to ours. They apply the code of Whitney et al. (2003b), which employs the same radiative equilibrium algorithm as in Bjorkman & Wood (2001), to hydrodynamic simulations of galaxy mergers with black holes. However, the spherical, logarithmically spaced grid used by these authors is not optimal for describing an inhomogeneous distribution of gas and dust with multiple density centers in galaxies and mergers, as exemplified by Figure 3. Moreover, our methodology is based on a treatment of the multiphase ISM that includes extinction from dust in the diffuse phase, which was ignored in the work of Chakrabarti et al. (2007a, 2007b). Furthermore, we adopt an AGN input spectrum that includes emission from dust on scales that the simulations do not resolve, unlike Chakrabarti et al. (2007a, 2007b), who employ a power-law AGN spectrum. The tests described above demonstrate that the near- and mid-IR emission is sensitive to the resolution of the RT calculation (Fig. 7), extinction by dust in the diffuse phase of the ISM (Fig. 8), and the template spectrum of the AGN (Fig. 10). The SEDs in the work of Chakrabarti et al. (2007a, 2007b) show only cold dust emission characteristic of a starburst during all evolutionary phases, even when the quasar peaks (e.g., Fig. 20 in Chakrabarti et al. 2007b), and, in particular, do not at any time exhibit hot dust emission. We attribute the differences between our computed SEDs and those of Chakrabarti et al. (2007a, 2007b) mainly to the different grid method employed, the handling of extinction by the diffuse ISM, and our choice of an AGN input spectrum that includes emission on scales that cannot be resolved in our hydrodynamic simulations.

In our radiative transfer calculations, we do not explicitly include a dust torus near the AGN. The resolution of our RT grid is constrained by that of the hydrodynamic simulations, which is of ~30 pc. As a result, we cannot resolve the near vicinity of the AGN. In the unification scheme for AGNs (Miller & Antonucci 1983), a parsec-scale dust torus, both optically and geometrically thick, has been used to successfully explain the different appearances of Type 1 and Type 2 AGNs. For example, Type 1 AGNs are typically viewed face-on and show blue UV bump in their spectra, while Type 2 AGNs are viewed edge-on without the blue UV bump. It is believed that the NIR and MIR emission of an AGN comes from the hot dust in the torus structure, as suggested by various observations, for examples, the MIR and NIR detection of a Seyfert 2 galaxy NGC 1068 (Jaffe et al. 2004; Wittkowski et al. 2004), and the MIR emission of a lensed quasar Q2237+0305 by Wyithe et al. (2002) in the CfA Redshift Survey (Huchra et al. 1985). The radiative transfer modeling by Hönig et al. (2006), which concentrates on the inner parsecs of the AGN, has successfully reproduced the SED of NGC 1068 in the NIR and MIR with a three-dimensional, clumpy dust torus. Such a scale is, however, below the resolution of our modeling, which follows the dynamical evolution of the quasar system on a galactic scale. Moreover, it is not clear whether such a well-defined torus structure would exist in luminous quasars at high redshifts. Nevertheless, we have adopted a composite AGN spectrum (Hopkins et al. 2007d) as a subresolution recipe for the IR emission from the hottest dust near the AGN. Such an approach is supported by the fact that the composite spectrum represents the average near- to mid-IR emission in thousands of quasars (Richards et al. 2006), and that the torus does not contribute much to the far-IR emission, which comes mainly from cold dust on kiloparsec scales. Therefore, for spatial scales of interest, the results should be reliable, and they are expected be similar to those from calculations with a torus included. We defer such a calculation to the future when subparsec resolution is feasible in hydrodynamic simulations of quasar formation.

We should point out that dust destruction is not explicitly included in our modeling. It has been suggested (e.g., McKee 1989; Draine & McKee 1993; Draine 2003; Nozawa et al. 2006) that dust destruction might be efficient in nonradiative shocks by nonthermal and thermal sputtering owing to a high shock velocity (>100 km s^{-1}) and a high gas temperature (>10^6 K). However, the sputtering timescale for this temperature is of $\sim 3 \times 10^6$ yr for a gas density $n = 1$ cm^{-1}, and even shorter if the gas density is higher (Burke & Silk 1974; Reynolds et al. 1997). It has also been suggested that dust grains may be destroyed behind radiative shocks (Todini & Ferrara 2001; Bianchi & Schneider 2007). However, it is expected that the efficiency cannot be significant at high redshifts as magnetic fields are likely weak (Gnedin et al. 2000). In our dust treatment in the RT analysis, the dust is recalculated based on the gas content in every snapshot from the hydrodynamic simulations, which has a time interval of 2 Myr. This is equivalent to dust destruction within this timescale. Moreover, we assume different dust-to-gas ratios for the cold and hot gas, which accounts for dust survival in these different phases of the interstellar medium.

One limitation of our ART^2 code is that it does not include the transient heating of small dust grains (size < 200 Å), which may cause temperature fluctuation and produce enhanced near-infrared emission (Li & Draine 2001; Misselt et al. 2001), in particular for the PAH feature. Although PAH is not studied in this present work, the code can be improved in the future by implementing a temperature distribution for those small grains. Moreover, one potential caveat of our RT work is that it is a postprocessing procedure. It would be ideal to couple the radiation with hydrodynamics; i.e., having the radiative transfer done simultaneously with the hydrodynamic simulations (as in e.g., Yoshida et al. 2007) as the dynamical evolution of the gas might affect the formation and properties of the dust. However, this effect is currently uncertain because such a technique is not yet available for dust emission in galaxy simulations. Although ART^2 is not parallelized, it works fairly efficiently owing to the adaptive refinement tree.

We have done extensive resolution studies which include both the number of photon packets and the refinement level of the grid, and parameters for the ISM model such as the cloud mass spectrum and size distribution, as well as different dust models. We find convergence of the modeled SEDs with parameters within observational ranges (see §§ 2 and 3). Therefore, we conclude that the RT calculations we present here with ART^2 are robust, and that our model is more self-consistent, more realistic, and more versatile than previous approaches.

8. SUMMARY

We have implemented a three-dimensional Monte Carlo radiative transfer code, ART^2—All-wavelength Radiative Transfer with Adaptive Refinement Tree—and use it to calculate the dust emission and multiwavelength properties of quasars and galaxies. ART^2 includes the following essential implementations:

1. A radiative equilibrium algorithm developed by Bjorkman & Wood (2001). It conserves the total photon energy, and corrects the dust temperature without iteration. This algorithm calculates dust emission efficiently and self-consistently.

2. An adaptive grid scheme in three-dimensional Cartesian coordinates similar to that of Jonsson (2006), which handles an arbitrary geometry and covers a large dynamic range over several orders of magnitude. This is indispensable for capturing the inhomogeneous and clumpy density distribution in galaxies and galaxy mergers. It easily achieves a ~10 pc scale grid resolution equivalent to a $\sim 10{,}000^3$ uniform grid, which is prohibitive with current computation schemes.

3. A two-phase ISM model in which the cold, dense clouds are embedded in a hot, diffuse medium in pressure equilibrium (Springel & Hernquist 2003a). Moreover, the cold clouds follow a mass spectrum and a size distribution similar to the Larson (1981) scaling relations inferred for giant molecular clouds. This model ensures an appropriate subgrid recipe for the ISM physics, which is important for studying dust properties in galaxies.

4. A supernova-origin dust model in which the dust is produced by Type II supernovae, and the size distribution of grains follows that derived by Todini & Ferrara (2001). This model may be especially relevant for dust in high-redshift, young objects. In traditional dust models, the dust is produced by old, low-mass stars such as AGB stars, which are typically over 1 Gyr old. However, quasar systems at ~6.4 are only a few hundred Myr old, and there would be insufficient AGB stars to produce the abundant dust observed in J1148+5251.

5. The input spectra include those from both stars, calculated using STARBURST99 (Leitherer et al. 1999; Vázquez & Leitherer 2005), and black holes represented by a composite AGN template developed by Hopkins et al. (2007d). The composite spectrum includes a broken power law as the intrinsic black hole spectrum, and infrared components that come from the torus near the AGN. The torus structure is unresolved in our hydrodynamic simulations. This template is a subgrid recipe to include the hot

dust emission within parsec scales, which is below the resolution of our hydrodynamic simulations.

ART^2 works efficiently on hydrodynamic simulations of galaxies and quasars performed with GADGET2 (Springel 2005). By applying ART^2 to the quasar simulations of Li et al. (2007) in which luminous quasars at $z \gtrsim 6$ form rapidly through hierarchical mergers of gas-rich galaxies, we are able to calculate the multiwavelength SEDs (from optical to millimeter) and dust properties of the model quasar at $z \sim 6.5$ and its galaxy progenitors at even higher redshifts.

We find that a supernova-origin dust model may be able to explain the dust properties observed in the high-redshift quasars. Our calculations reproduce the observed SED and properties such as the dust mass and temperature of J1148+5251, the most distant Sloan quasar. The dust and infrared emission in quasar hosts are closely associated with the formation and evolution of the system. As the system transforms from starburst to quasar phases, the evolution of the SEDs is characterized by a transition from a cold to warm ULIRG. During the starburst phase at $z \gtrsim 7.5$, the SEDs of the quasar progenitors exhibit cold dust bumps (peak at $\sim$50 μm rest frame) that are characteristic of starburst galaxies. During the peak quasar phase ($z \sim 7.5$–6), the SEDs show a prominent hot dust bump (peaks at $\sim$3 μm rest frame), as observed in luminous quasars at both low and high redshifts (e.g., Richards et al. 2006; Jiang et al. 2006).

Furthermore, we find that during the quasar phase, AGN activity dominates the heating of dust and the resulting infrared luminosities. This has significant implications for the interpretation of observables from the quasar host. The hottest dust ($T \gtrsim 10^3$ K) is present only during the peak quasar activity, and correlates strongly with the near-IR flux. The SFR-$L_{\rm FIR}$ correlation depends sensitively on the relative heating contributed from AGN and stars. If the dust heating is dominated by stars, as in the starburst phase, then there is a tight, linear SFR-$L_{\rm FIR}$ correlation similar to the one widely used to interpret observations (Kennicutt 1998b). However, if both AGN and stars contribute to the dust emission in the far-IR, then the correlation becomes nonlinear with a modified normalization. If the AGN dominates the $L_{\rm FIR}$, as in the peak quasar phase, we find no correlation at all. Finally, we find correlations between dust masses and rest-frame fluxes at 3 and 50 μm. The $f_{3\ \mu{\rm m}}$ flux may serve as a good diagnostic for hot dust in quasars, while $f_{50\ \mu{\rm m}}$ may be used to estimate the amount of cold dust in starburst galaxies, as $f_{50\ \mu{\rm m}}$ correlates linearly with the cold dust mass.

Our model demonstrates that massive star formation at higher redshifts ($z \gtrsim 10$) is necessary in order to produce the observed dust properties in these quasars. This suggests that the quasar hosts should have already built up a large stellar population by $z \sim 6$. Our results support a merger-driven origin for luminous quasars at high redshifts, and provide further evidence for the hypothesis of starburst-to-quasar evolution.

Special thanks to Kenny Wood[6] and Barbara Whitney[7] for generously making their Monte Carlo radiative equilibrium codes publicly available; and to Patrik Jonsson for sharing publicly his fantastic radiative transfer code SUNRISE.[8] We thank Gurtina Besla, Stephanie Bush, Sukanya Chakrabarti, Suvendra Dutta, Giovanni Fazio, Jiasheng Huang, Dusan Keres, Desika Narayanan, Erik Rosolowsky, and Josh Younger for many stimulating discussions. Y. L. thanks Lee Armus, Frank Bertoldi, Bruce Draine, Patrik Jonsson, Carol Lonsdale, Mike Nolta, Casey Papovich, George Rybicki, Nick Scoville, Rodger Thompson, and Lin Yan for inspiration and discussions. Finally, we thank the referee for a thoughtful report that has helped improve this manuscript. Y. L. gratefully acknowledges a Keck Fellowship sponsored by the Keck Foundation, as well as an Institute for Theory and Computation Fellowship, under which support most of this work was done. The computations reported here were performed at the Center for Parallel Astrophysical Computing at Harvard-Smithsonian Center for Astrophysics. This work was supported in part by NSF grant 03-07690 and NASA ATP grant NAG5-13381.

[6] See http://www-star.st-and.ac.uk/~kw25/research/montecarlo/montecarlo.html.

[7] See http://gemelli.colorado.edu/~bwhitney/codes/codes.html.

[8] See http://www.ucolick.org/~patrik/sunrise.

REFERENCES

Abel, T., Bryan, G. L., & Norman, M. L. 2002, Science, 295, 93
Andre, P., Ward-Thompson, D., & Motte, F. 1996, A&A, 314, 625
Armus, L., et al. 2004, ApJS, 154, 178
Baes, M., Stamatellos, D., Davies, J. I., Whitworth, A. P., Sabatini, S., Roberts, S., Linder, S. M., & Evans, R. 2005, NewA, 10, 523
Ballesteros-Paredes, J., & Mac Low, M.-M. 2002, ApJ, 570, 734
Barnes, J. E., & Hernquist, L. 1992, ARA&A, 30, 705
———. 1991, ApJ, 370, L65
———. 1996, ApJ, 471, 115
Barth, A. J., Martini, P., Nelson, C. H., & Ho, L. C. 2003, ApJ, 594, L95
Beelen, A., Cox, P., Benford, D. J., Dowell, C. D., Kovács, A., Bertoldi, F., Omont, A., & Carilli, C. L. 2006, ApJ, 642, 694
Bertoldi, F., Carilli, C. L., Cox, P., Fan, X., Strauss, M. A., Beelen, A., Omont, A., & Zylka, R. 2003a, A&A, 406, L55
Bertoldi, F., et al. 2003b, A&A, 409, L47
Bianchi, S., Ferrara, A., Davies, J. I., & Alton, P. B. 2000, MNRAS, 311, 601
Bianchi, S., & Schneider, R. 2007, MNRAS, 378, 973
Bjorkman, J. E., & Wood, K. 2001, ApJ, 554, 615
Blitz, L., Fukui, Y., Kawamura, A., Leroy, A., Mizuno, N., & Rosolowsky, E. 2007, in Protostars and Planets V, ed. B. Reipurth, D. Jewitt, & K. Keil (Univ. Arizona Press: Tucson), 81
Blitz, L., & Rosolowsky, E. 2006, ApJ, 650, 933
Bondi, H. 1952, MNRAS, 112, 195
Bondi, H., & Hoyle, F. 1944, MNRAS, 104, 273
Brand, K., et al. 2006, ApJ, 644, 143
Brandt, W. N., et al. 2002, ApJ, 569, L5
Bromm, V., & Larson, R. B. 2004, ARA&A, 42, 79
Burke, J. R., & Silk, J. 1974, ApJ, 190, 1
Calzetti, D., Armus, L., Bohlin, R. C., Kinney, A. L., Koornneef, J., & Storchi-Bergmann, T. 2000, ApJ, 533, 682
Calzetti, D., Kinney, A. L., & Storchi-Bergmann, T. 1994, ApJ, 429, 582
Carilli, C. L., et al. 2001, ApJ, 555, 625
———. 2004, AJ, 128, 997
Chakrabarti, S., Cox, T. J., Hernquist, L., Hopkins, P. F., Robertson, B., & Di Matteo, T. 2007a, ApJ, 658, 840
Chakrabarti, S., et al. 2007b, ApJ, submitted (astro-ph/0610860)
Charmandaris, V., et al. 2004, ApJS, 154, 142
Code, A. D., & Whitney, B. A. 1995, ApJ, 441, 400
Colgan, S. W. J., Haas, M. R., Erickson, E. F., Lord, S. D., & Hollenbach, D. J. 1994, ApJ, 427, 874
Condon, J. J. 1992, ARA&A, 30, 575
Dame, T. M., Elmegreen, B. G., Cohen, R. S., & Thaddeus, P. 1986, ApJ, 305, 892
Di Matteo, T., Colberg, J., Springel, V., Hernquist, L., & Sijacki, D. 2008, ApJ, 676, 33
Di Matteo, T., Springel, V., & Hernquist, L. 2005, Nature, 433, 604
Dorschner, J., & Henning, T. 1995, Astron. Astrophys. Rev., 6, 271
Draine, B. T. 2003, ARA&A, 41, 241
Draine, B. T., & Lazarian, A. 1998, ApJ, 508, 157
Draine, B. T., & Li, A. 2001, ApJ, 551, 807
———. 2007, ApJ, 657, 810
Draine, B. T., & McKee, C. F. 1993, ARA&A, 31, 373
Dullemond, C. P., & Turolla, R. 2000, A&A, 360, 1187
Dunne, L., Eales, S., Ivison, R., Morgan, H., & Edmunds, M. 2003, Nature, 424, 285

Dunne, L., & Eales, S. A. 2001, MNRAS, 327, 697
Dwek, E. 2004, ApJ, 607, 848
———. 2005, in AIP Conf. Proc. 761, The Spectral Energy Distributions of Gas-Rich Galaxies: Confronting Models with Data, ed. C. C. Popescu & R. J. Tuffs (Melville: AIP), 103
Dwek, E., Galliano, F., & Jones, A. P. 2007, ApJ, 662, 927
Efstathiou, A., & Rowan-Robinson, M. 1990, MNRAS, 245, 275
———. 1991, MNRAS, 252, 528
Elmegreen, B. G. 1989, ApJ, 338, 178
———. 2002, ApJ, 564, 773
Elmegreen, B. G., & Falgarone, E. 1996, ApJ, 471, 816
Elvis, M., Marengo, M., & Karovska, M. 2002, ApJ, 567, L107
Elvis, M., et al. 1994, ApJS, 95, 1
Fan, X. 2006, Mem. Soc. Astron. Italiana, 77, 635
Fan, X., Carilli, C. L., & Keating, B. 2006a, ARA&A, 44, 415
Fan, X., et al. 2003, AJ, 125, 1649
———. 2004, AJ, 128, 515
———. 2006b, AJ, 132, 117
Finkbeiner, D. P. 1999, Ph.D. thesis, Univ. California (Berkeley)
Finkbeiner, D. P., Davis, M., & Schlegel, D. J. 1999, ApJ, 524, 867
Finkbeiner, D. P., Schlegel, D. J., Frank, C., & Heiles, C. 2002, ApJ, 566, 898
Folini, D., Walder, R., Psarros, M., & Desboeufs, A. 2003, in ASP Conf. Ser. 288, Stellar Atmosphere Modeling, ed. I. Hubeny, D. Mihalas, & K. Werner(San Francisco: ASP), 433
Freudling, W., Corbin, M. R., & Korista, K. T. 2003, ApJ, 587, L67
Fuller, G. A., & Myers, P. C. 1992, ApJ, 384, 523
Gao, L., White, S. D. M., Jenkins, A., Frenk, C. S., & Springel, V. 2005, MNRAS, 363, 379
Gao, L., Yoshida, N., Abel, T., Frenk, C. S., Jenkins, A., & Springel, V. 2007, MNRAS, 378, 449
Gehrz, R. 1989, in IAU Symp. 135, Interstellar Dust, ed. L. J. Allamandola & A. G. G. M. Tielens (Dordrecht: Kluwer), 445
Gehrz, R. D., & Ney, E. P. 1987, Proc. Natl. Acad. Sci., 84, 6961
Glikman, E., Helfand, D. J., & White, R. L. 2006, ApJ, 640, 579
Gnedin, N. Y., Ferrara, A., & Zweibel, E. G. 2000, ApJ, 539, 505
Gunn, J. E., & Peterson, B. A. 1965, ApJ, 142, 1633
Haas, M., et al. 2003, A&A, 402, 87
Hall, P. B., Gallagher, S. C., Richards, G. T., Alexander, D. M., Anderson, S. F., Bauer, F., Brandt, W. N., & Schneider, D. P. 2006, AJ, 132, 1977
Hao, L., Weedman, D. W., Spoon, H. W. W., Marshall, J. A., Levenson, N. A., Elitzur, M., & Houck, J. R. 2007, ApJ, 655, L77
Hao, L., et al. 2005, ApJ, 625, L75
Harries, T. J. 2000, MNRAS, 315, 722
Harries, T. J., Monnier, J. D., Symington, N. H., & Kurosawa, R. 2004, MNRAS, 350, 565
Hernquist, L. 1989, Nature, 340, 687
———. 1990, ApJ, 356, 359
Hernquist, L., & Katz, N. 1989, ApJS, 70, 419
Hernquist, L., & Mihos, J. C. 1995, ApJ, 448, 41
Hines, D. C., Krause, O., Rieke, G. H., Fan, X., Blaylock, M., & Neugebauer, G. 2006, ApJ, 641, L85
Hirashita, H., Nozawa, T., Kozasa, T., Ishii, T. T., & Takeuchi, T. T. 2005, MNRAS, 357, 1077
Hönig, S. F., Beckert, T., Ohnaka, K., & Weigelt, G. 2006, A&A, 452, 459
Hopkins, P. F., Cox, T. J., Keres, D., & Hernquist, L. 2007a, preprint (arXiv: 0706.1246)
Hopkins, P. F., Hernquist, L., Cox, T. J., Di Matteo, T., Martini, P., Robertson, B., & Springel, V. 2005a, ApJ, 630, 705
Hopkins, P. F., Hernquist, L., Cox, T. J., Di Matteo, T., Robertson, B., & Springel, V. 2005b, ApJ, 630, 716
———. 2006, ApJS, 163, 1
Hopkins, P. F., Hernquist, L., Cox, T. J., & Keres, D. 2007b, preprint (arXiv: 0706.1243)
Hopkins, P. F., Hernquist, L., Cox, T. J., Robertson, B., & Krause, E. 2007c, ApJ, 669, 67
Hopkins, P. F., Hernquist, L., Martini, P., Cox, T. J., Robertson, B., Di Matteo, T., & Springel, V. 2005c, ApJ, 625, L71
Hopkins, P. F., Richards, G. T., & Hernquist, L. 2007d, ApJ, 654, 731
Hopkins, P. F., et al. 2004, AJ, 128, 1112
Houck, J. R., et al. 2004, ApJS, 154, 18
———. 2005, ApJ, 622, L105
Huchra, J., Gorenstein, M., Kent, S., Shapiro, I., Smith, G., Horine, E., & Perley, R. 1985, AJ, 90, 691
Hughes, D. H., Dunlop, J. S., & Rawlings, S. 1997, MNRAS, 289, 766
Hummer, D. G., & Rybicki, G. B. 1971, MNRAS, 152, 1
Ivezić, Ž., Groenewegen, M. A. T., Men'shchikov, A., & Szczerba, R. 1997, MNRAS, 291, 121
Jaffe, W., et al. 2004, Nature, 429, 47
Jiang, L., et al. 2006, AJ, 132, 2127
Jonsson, P. 2006, MNRAS, 372, 2
Kennicutt, R. C. 1998a, ApJ, 498, 541
———. 1998b, ARA&A, 36, 189
Kim, S.-H., Martin, P. G., & Hendry, P. D. 1994, ApJ, 422, 164
Klaas, U., et al. 2001, A&A, 379, 823
Krause, O., Birkmann, S. M., Rieke, G. H., Lemke, D., Klaas, U., Hines, D. C., & Gordon, K. D. 2004, Nature, 432, 596
Kroupa, P. 2002, Science, 295, 82
Kuraszkiewicz, J. K., et al. 2003, ApJ, 590, 128
Kurosawa, R., & Hillier, D. J. 2001, A&A, 379, 336
Laor, A., & Draine, B. T. 1993, ApJ, 402, 441
Larson, R. B. 1981, MNRAS, 194, 809
Lefevre, J., Bergeat, J., & Daniel, J.-Y. 1982, A&A, 114, 341
Lefevre, J., Daniel, J.-Y., & Bergeat, J. 1983, A&A, 121, 51
Leitherer, C., et al. 1999, ApJS, 123, 3
Leung, C. M. 1976, ApJ, 209, 75
Levenson, N. A., Sirocky, M. M., Hao, L., Spoon, H. W. W., Marshall, J. A., Elitzur, M., & Houck, J. R. 2007, ApJ, 654, L45
Li, A., & Draine, B. T. 2001, ApJ, 550, L213
———. 2002, ApJ, 572, 232
Li, Y., Klessen, R. S., & Mac Low, M.-M. 2003, ApJ, 592, 975
Li, Y., Mac Low, M.-M., & Klessen, R. S. 2004, ApJ, 614, L29
———. 2005a, ApJ, 620, L19
———. 2005b, ApJ, 626, 823
———. 2006, ApJ, 639, 879
Li, Y., et al. 2007, ApJ, 655, 187
Lopez, B., Mekarnia, D., & Lefevre, J. 1995, A&A, 296, 752
Lucy, L. B. 1999, A&A, 344, 282
Madau, P. 1995, ApJ, 441, 18
Magorrian, J., et al. 1998, AJ, 115, 2285
Maiolino, R., Marconi, A., Salvati, M., Risaliti, G., Severgnini, P., Oliva, E., La Franca, F., & Vanzi, L. 2001, A&A, 365, 28
Maiolino, R., Schneider, R., Oliva, E., Bianchi, S., Ferrara, A., Mannucci, F., Pedani, M., & Roca Sogorb, M. 2004, Nature, 431, 533
Maiolino, R., et al. 2006, Mem. Soc. Astron. Italiana, 77, 643
Marchenko, S. V. 2006, in ASP Conf. Ser. 353, Stellar Evolution at Low Metallicity: Mass Loss, Explosions, Cosmology, ed. H. J. G. L. M. Lamers et al. (San Francisco: ASP), 299
Marconi, A., & Hunt, L. K. 2003, ApJ, 589, L21
Marconi, A., Risaliti, G., Gilli, R., Hunt, L. K., Maiolino, R., & Salvati, M. 2004, MNRAS, 351, 169
Mathis, J. S. 1990, ARA&A, 28, 37
Mathis, J. S., Rumpl, W., & Nordsieck, K. H. 1977, ApJ, 217, 425
McKee, C. 1989, in IAU Symp. 135, Interstellar Dust, ed. L. J. Allamandola & A. G. G. M. Tielens (Dordrecht: Kluwer), 431
McKee, C. F., & Ostriker, J. P. 1977, ApJ, 218, 148
Men'shchikov, A. B., & Henning, T. 1997, A&A, 318, 879
Mihos, J. C., & Hernquist, L. 1996, ApJ, 464, 641
Miller, J. S., & Antonucci, R. R. J. 1983, ApJ, 271, L7
Misselt, K. A., Gordon, K. D., Clayton, G. C., & Wolff, M. J. 2001, ApJ, 551, 277
Morgan, H. L., Dunne, L., Eales, S. A., Ivison, R. J., & Edmunds, M. G. 2003, ApJ, 597, L33
Morgan, H. L., & Edmunds, M. G. 2003, MNRAS, 343, 427
Moseley, S. H., Dwek, E., Glaccum, W., Graham, J. R., & Loewenstein, R. F. 1989, Nature, 340, 697
Narayanan, D., Kulesa, C., Boss, A., & Walker, C. K. 2006a, ApJ, 647, 1246
Narayanan, D., et al. 2007, ApJ, submitted
———. 2006b, ApJ, 642, L107
Nenkova, M., Ivezić, Ž., & Elitzur, M. 2002, ApJ, 570, L9
Norman, C., & Scoville, N. 1988, ApJ, 332, 124
Nozawa, T., Kozasa, T., & Habe, A. 2006, ApJ, 648, 435
Nozawa, T., Kozasa, T., Habe, A., Dwek, E., Umeda, H., Tominaga, N., Maeda, K., & Nomoto, K. 2007, ApJ, 666, 955
Nozawa, T., Kozasa, T., Umeda, H., Maeda, K., & Nomoto, K. 2003, ApJ, 598, 785
Papovich, C., et al. 2006, ApJ, 640, 92
Pascucci, I., Wolf, S., Steinacker, J., Dullemond, C. P., Henning, T., Niccolini, G., Woitke, P., & Lopez, B. 2004, A&A, 417, 793
Pentericci, L., et al. 2003, A&A, 410, 75
Pinte, C., Ménard, F., Duchêne, G., & Bastien, P. 2006, A&A, 459, 797
Polletta, M., Courvoisier, T. J.-L., Hooper, E. J., & Wilkes, B. J. 2000, A&A, 362, 75
Reynolds, C. S., Ward, M. J., Fabian, A. C., & Celotti, A. 1997, MNRAS, 291, 403
Rice, W. K. M., Wood, K., Armitage, P. J., Whitney, B. A., & Bjorkman, J. E. 2003, MNRAS, 342, 79

Richards, G. T., et al. 2006, ApJS, 166, 470
Rieke, G. H., & Lebofsky, M. J. 1981, ApJ, 250, 87
Robertson, B., Hernquist, L., Cox, T. J., Di Matteo, T., Hopkins, P. F., Martini, P., & Springel, V. 2006, ApJ, 641, 90
Robertson, B., Li, Y., Cox, T. J., Hernquist, L., & Hopkins, P. F. 2007, ApJ, 667, 60
Robson, I., Priddey, R. S., Isaak, K. G., & McMahon, R. G. 2004, MNRAS, 351, L29
Roche, P. F., Aitken, D. K., & Smith, C. H. 1993, MNRAS, 261, 522
Rosolowsky, E. 2005, PASP, 117, 1403
———. 2007, ApJ, 654, 240
Rowan-Robinson, M. 1980, ApJS, 44, 403
Salpeter, E. E. 1955, ApJ, 121, 161
Sanders, D. B., & Mirabel, I. F. 1996, ARA&A, 34, 749
Sanders, D. B., Scoville, N. Z., & Solomon, P. M. 1985, ApJ, 289, 373
Sanders, D. B., Soifer, B. T., Elias, J. H., Madore, B. F., Matthews, K., Neugebauer, G., & Scoville, N. Z. 1988, ApJ, 325, 74
Savage, B. D., & Mathis, J. S. 1979, ARA&A, 17, 73
Schlegel, D. J., Finkbeiner, D. P., & Davis, M. 1998, ApJ, 500, 525
Schmidt, M. 1959, ApJ, 129, 243
Schneider, R., Ferrara, A., & Salvaterra, R. 2004, MNRAS, 351, 1379
Scoville, N. 2003, J. Korean Astron. Soc., 36, 167
Scoville, N. Z., & Kwan, J. 1976, ApJ, 206, 718
Scoville, N. Z., Yun, M. S., Sanders, D. B., Clemens, D. P., & Waller, W. H. 1987, ApJS, 63, 821
Shemmer, O., et al. 2006, ApJ, 644, 86
Shemmer, O., Brandt, W. N., Vignali, C., Schneider, D. P., Fan, X., Richards, G. T., & Strauss, M. A. 2005, ApJ, 630, 729
Siebenmorgen, R., Haas, M., Krügel, E., & Schulz, B. 2005, A&A, 436, L5
Siebenmorgen, R., & Krügel, E. 2007, A&A, 461, 445
Sijacki, D., Springel, V., Di Matteo, T., & Hernquist, L. 2007, MNRAS, 380, 877
Solomon, P. M., Rivolo, A. R., Barrett, J., & Yahil, A. 1987, ApJ, 319, 730
Spergel, D. N., et al. 2003, ApJS, 148, 175
Spoon, H. W. W., Marshall, J. A., Houck, J. R., Elitzur, M., Hao, L., Armus, L., Brandl, B. R., & Charmandaris, V. 2007, ApJ, 654, L49
Spoon, H. W. W., Moorwood, A. F. M., Lutz, D., Tielens, A. G. G. M., Siebenmorgen, R., & Keane, J. V. 2004, A&A, 414, 873
Spoon, H. W. W., et al2006, ApJ, 638, 759
Springel, V. 2005, MNRAS, 364, 1105
Springel, V., Di Matteo, T., & Hernquist, L. 2005a, MNRAS, 361, 776
Springel, V., & Hernquist, L. 2002, MNRAS, 333, 649
———. 2003a, MNRAS, 339, 289
———. 2003b, MNRAS, 339, 312
Springel, V., et al. 2005b, Nature, 435, 629
Spyromilio, J., Stathakis, R. A., & Meurer, G. R. 1993, MNRAS, 263, 530
Steffen, A. T., Strateva, I., Brandt, W. N., Alexander, D. M., Koekemoer, A. M., Lehmer, B. D., Schneider, D. P., & Vignali, C. 2006, AJ, 131, 2826
Steinacker, J., Bacmann, A., & Henning, T. 2006, ApJ, 645, 920
Steinacker, J., Henning, T., Bacmann, A., & Semenov, D. 2003, A&A, 401, 405
Strateva, I. V., Brandt, W. N., Schneider, D. P., Vanden Berk, D. G., & Vignali, C. 2005, AJ, 130, 387
Stratta, G., Maiolino, R., Fiore, F., & D'Elia, V. 2007, ApJ, 661, L9
Sturm, E., Lutz, D., Tran, D., Feuchtgruber, H., Genzel, R., Kunze, D., Moorwood, A. F. M., & Thornley, M. D. 2000, A&A, 358, 481
Sturm, E., et al. 2005, ApJ, 629, L21
Sugerman, B. E. K., et al. 2006, Science, 313, 196
Tan, J. C., & McKee, C. F. 2004, ApJ, 603, 383
Telfer, R. C., Zheng, W., Kriss, G. A., & Davidsen, A. F. 2002, ApJ, 565, 773
Todini, P., & Ferrara, A. 2001, MNRAS, 325, 726
Vanden Berk, D. E., Richards, G. T., & Bauer, A. 2001, AJ, 122, 549
Vázquez, G. A., & Leitherer, C. 2005, ApJ, 621, 695
Vignali, C., Brandt, W. N., Schneider, D. P., Garmire, G. P., & Kaspi, S. 2003, AJ, 125, 418
Vignali, C., Brandt, W. N., Schneider, D. P., & Kaspi, S. 2005, AJ, 129, 2519
Walter, F., et al. 2003, Nature, 424, 406
———. 2004, ApJ, 615, L17
Wang, R., et al. 2007, AJ, 134, 617
Ward-Thompson, D., Scott, P. F., Hills, R. E., & Andre, P. 1994, MNRAS, 268, 276
Weingartner, J. C., & Draine, B. T. 2001, ApJ, 548, 296
Werner, M. W., et al. 2004, ApJS, 154, 1
White, R. L., Becker, R. H., Fan, X., & Strauss, M. A. 2005, AJ, 129, 2102
Whitney, B. A., & Hartmann, L. 1992, ApJ, 395, 529
———. 1993, ApJ, 402, 605
Whitney, B. A., Indebetouw, R., Bjorkman, J. E., & Wood, K. 2004, ApJ, 617, 1177
Whitney, B. A., Wood, K., Bjorkman, J. E., & Cohen, M. 2003a, ApJ, 598, 1079
Whitney, B. A., Wood, K., Bjorkman, J. E., & Wolff, M. J. 2003b, ApJ, 591, 1049
Whittet, D. C. B., ed. 2003, Dust in the Galactic Environment (Bristol: IOP)
Willott, C. J., McLure, R. J., & Jarvis, M. J. 2003, ApJ, 587, L15
Willott, C. J., Percival, W. J., McLure, R. J., Crampton, D., Hutchings, J. B., Jarvis, M. J., Sawicki, M., & Simard, L. 2005, ApJ, 626, 657
Willott, C. J., et al. 2007, AJ, 134, 2435
Witt, A. N. 1977, ApJS, 35, 1
Witt, A. N., Thronson, H. A., Jr., & Capuano, Jr., J. M. 1992, ApJ, 393, 611
Wittkowski, M., Kervella, P., Arsenault, R., Paresce, F., Beckert, T., & Weigelt, G. 2004, A&A, 418, L39
Wolf, S., Henning, T., & Stecklum, B. 1999, A&A, 349, 839
Wolfire, M. G., & Cassinelli, J. P. 1986, ApJ, 310, 207
Wood, K., Bjorkman, J. E., Whitney, B., & Code, A. 1996a, ApJ, 461, 847
———. 1996b, ApJ, 461, 828
Wood, K., & Jones, T. J. 1997, AJ, 114, 1405
Wood, K., Kenyon, S. J., Whitney, B., & Turnbull, M. 1998, ApJ, 497, 404
Wood, K., Lada, C. J., Bjorkman, J. E., Kenyon, S. J., Whitney, B., & Wolff, M. J. 2002, ApJ, 567, 1183
Wood, K., & Loeb, A. 2000, ApJ, 545, 86
Wyithe, J. S. B., Agol, E., & Fluke, C. J. 2002, MNRAS, 331, 1041
York, D. G., Adelman, J., & Anderson, Jr., J. E., et al. 2000, AJ, 120, 1579
Yorke, H. W. 1980, A&A, 86, 286
Yoshida, N., Abel, T., Hernquist, L., & Sugiyama, N. 2003, ApJ, 592, 645
Yoshida, N., Oh, S. P., Kitayama, T., & Hernquist, L. 2007, ApJ, 663, 687
Yoshida, N., Omukai, K., Hernquist, L., & Abel, T. 2006, ApJ, 652, 6